Precambrian Research 353 (2021) 106015

Contents lists available at ScienceDirect

Precambrian Research

journal homepage: www.elsevier.com/locate/precamres

Neoproterozoic *syn*-collision magmatism in the Nkondjock region at the northern border of the Congo craton in Cameroon: Geodynamic implications for the Central African orogenic belt

M.S Kamguia Kamani [a,b], Wei Wang [a,*], J.-P Tchouankoue [b], Si-Fang Huang [a], B Yomeun [a,b], Er-Kun Xue [a], Gui-Mei Lu [a]

[a] State Key Laboratory of Geological Processes and Mineral Resources, School of Earth Sciences, China University of Geosciences, Wuhan 430074, China
[b] Department of Earth Sciences, University of Yaoundé I, P.O. Box 812, Yaoundé, Cameroon

ARTICLE INFO

Keywords:
West Cameroon
Central African Orogenic belt
S- and I-type granitoids
Petrogenesis
Geodynamic implications

ABSTRACT

The Nkondjock area located in Western Cameroon is part of the Neoproterozoic Central African orogenic belt, at the northern border of the Congo craton. Rocks of the Nkondjock area are: two-mica orthogneisses, two-pyroxene orthogneisses and mylonitic orthogneisses. The protolith of two-mica, two-pyroxene and mylonitic orthogneisses crystallized at 607 ± 4, 624.4 ± 3.5 and 621 ± 9.1 Ma, respectively, and are thus consistent with the Central African Orogenic belt. Inherited zircons (2043 ± 27 Ma) of mylonitic orthogneisses are interpreted as an inherited age of the metacratonization of the northern border of the Congo craton. S-type affinity of two-mica orthogneisses together with two-pyroxene orthogneisses (Mabombé) display geochemical affinities typical of adakite, including high La/Yb_N (29.7–55.6) and low Y (3.43–6.69 ppm) with low Mg# (30.8–55), εNd(t) (−8.6 to −6.5), high $^{87}Sr/^{86}Sri$ (0.70684–0.71063) and positive εHf(t) (+3 to +4.9), similar to those adakites formed by partial melting of thickened lower crust with some mantle input. Two-pyroxene orthogneisses (Ndogboni) and mylonitic orthogneisses display I-type granitoids affinity with A/CNK (0.93–1.06) and are depleted in Nb, Ta, Sr, P, Ti and enriched in Rb, Th, and Pb. They also have low εNd(t) (−10.3 to −11), high $^{87}Sr/^{86}Sr_i$ (0.71017–0.71063) and negative εHf(t) (−19.1 to −1) similar to melts derived from mature continental crust. Sr-Nd-Hf isotopes confirm heterogeneous source for these orthogneisses with bimodal distribution on εHf(t) and εNd(t) values, suggesting mixing between juvenile mafic melt and a mature continental crust during the evolution of the Central African Orogenic belt. We suggest that the protolith of these orthogneisses (S- and I-type granitoids) were formed during *syn*-collisional setting between the Congo and the West African craton which followed a subduction through partial melting of a thickened lower continental crust due to a thermal anomaly induced by upwelling of asthenosphere through slab break-off.

1. Introduction

The Cameroon territory straddles the northern border of the Congo craton and the adjacent central African fold belt (CAFB) (Njonfang et al., 2006; Nkoumbou et al., 2014; Toteu et al., 2001). While the Proterozoic domain is relatively well known and underlined by an abundant plutonic activity (Djouka-Fonkwé et al., 2008; Kwékam et al., 2010; Njiekak et al., 2008; Tchameni et al., 2006; Tchouankoue et al., 2016), the tectonic evolution of the northern end of the Congo craton is still poorly understood for it was strongly deformed and reworked during the period of Eburnean and Pan-African orogenies. Recent studies have advanced our understanding of the Archean-Proterozoic transition in Cameroon (Tchakounté et al., 2017 and reference there in). Notably, (Ganwa et al., 2016) and (Tchakounté et al., 2017) obtained Archean ages (3.0–2.5 Ga) on gneisses in Adamawa and Bafia regions, respectively, suggesting that those regions were part of the northern margin of the Congo craton. In such a perspective, former extension of the Congo craton in Bafia and Adamawa regions, the boundary region between the Congo craton and the Proterozoic belt of West Cameroon narrows in Central and West Cameroon, to the tectonized corridor of lineaments with regional importance (Adamawa Shear Zone, ASZ; Tcholliré Banyo Fault, TBF) are thought to have reworked throughout of the Phanerozoic

* Corresponding Author.
E-mail address: wwz@cug.edu.cn (W. Wang).

https://doi.org/10.1016/j.precamres.2020.106015
Received 19 April 2020; Received in revised form 16 August 2020; Accepted 7 November 2020
Available online 24 November 2020
0301-9268/© 2020 Elsevier B.V. All rights reserved.

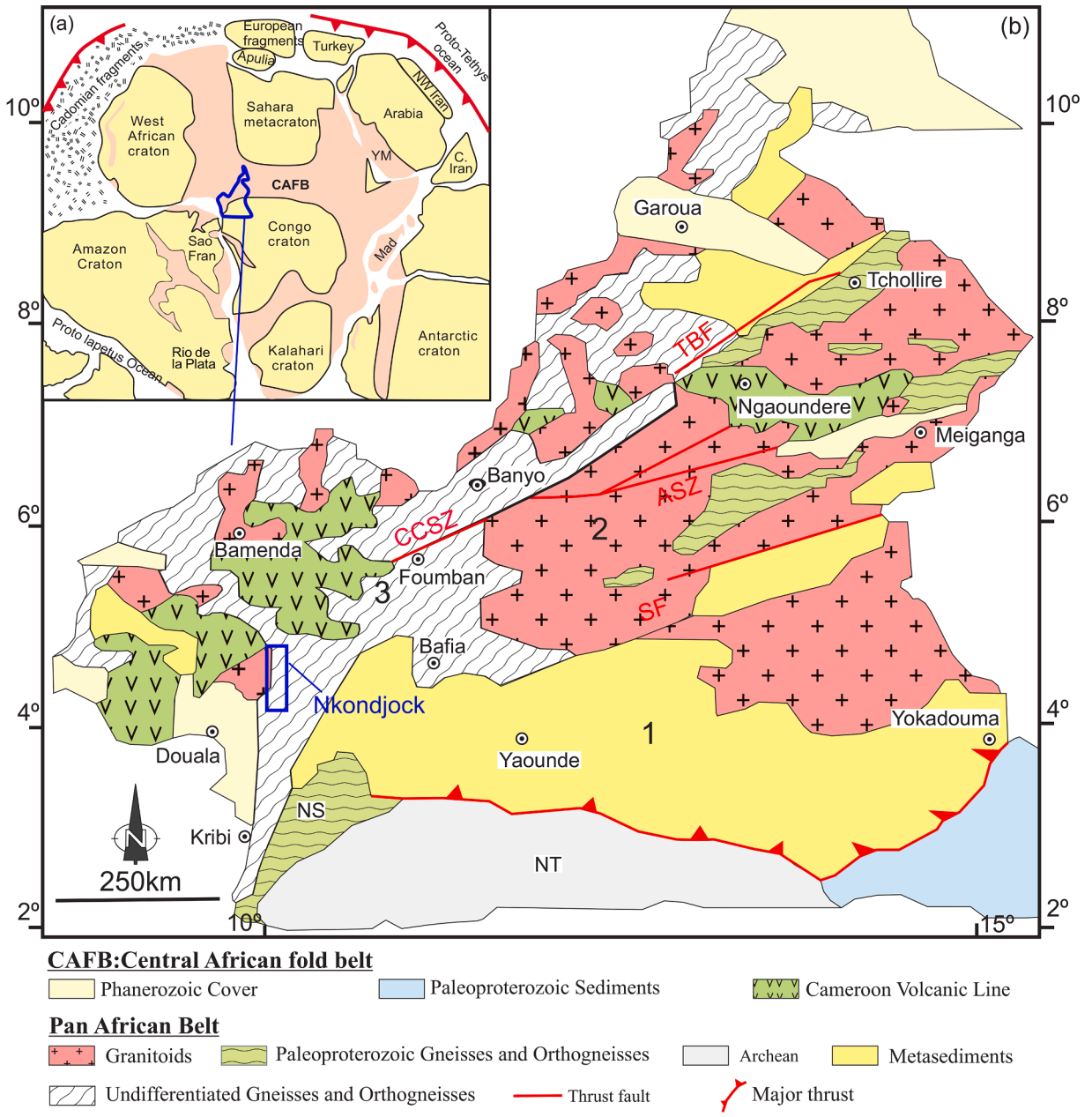

Fig. 1. (a) Reconstruction of a part of the Gondwana supercontinent, approximately 544 Ma ago (Modified after (Fitzsimons, 2003; Kusky et al., 2003) and references therein); (1b) Geological sketch map, of Cameroon with indication of the study area (frame), numbers in map indicate different domains: 1 southern domain (SD) corresponding to the Yaoundé series thrusted on the Congo Craton, 2 central domain (CD), 3 northern domain (ND). CCSZ: Central Cameroon Shear Zone; DS: Dja series; NS: Nyong series; NT: Ntem Complex; SF: Sanaga Fault; TBF: Tcholliré-Banyo Fault; ASZ: Adamawa shear zone.

(Simeni et al., 2017; Tchouankoue et al., 2014). Recent description on metabasites with MORB affinities in the Nyong series at the SSW of our area of study (Houketchang Bouyo et al., 2019; Loose and Schenk, 2018) brought convincing clues of an existence of a subduction environment in the Paleoproterozoic at the northern border of the Congo craton. Geochemical studies of late orogenic granitoids of West Cameroon that crop out abundantly in the NW of the Nkondjock area revealed many characteristics of production in a subduction environment: metaluminous to slightly peraluminous; calc-alkaline affinities, high LILE, negative anomalies in Nb and Ti on rocks vs primordial mantle normalization diagrams; oldest Nd TDM ages in the Paleoproterozoic (Djouka-Fonkwé et al., 2008; Njiekak et al., 2008; Tchouankoue et al., 2016; Ngo Belnoun et al., 2013). Zircons U/Pb geochronological results for granitoids of West Cameroon (Li et al., 2017; Njiekak et al., 2008; Kwékam et al., 2020) coupled with the regional tectonic studies (Tchameni et al., 2006; Kwékam et al., 2010; Nomo et al., 2017) provide clues for better understanding of the Pan-African domain of West Cameroon. Four tectonic phases have thus been identified: The D1 phase (>630 Ma) corresponds to initial magmatic episode followed by orthogneissification (Tchakounté et al., 2017), the D2 deformation phase (630–600 Ma) characterized by *syn*-collisional granitoids (Kwékam et al., 2020), the D3 phase (600–565) characterized by NE-SW transcurrent movements associated with production of dominant shoshonitic plutons (Tchouankoue et al., 2016); the D4 phase (ca. 560 Ma) constrained by the formation of the ca. 561 Ma *syn*-tectonic two-mica granite and the ca. 557 Ma undeformed biotite granite (Li et al., 2017).

In spite of the subduction signatures in Pan-African granitoids of West Cameroon, a reconstitution of complete Wilson cycle integrating these granitoids has not yet been done at the northern border of the

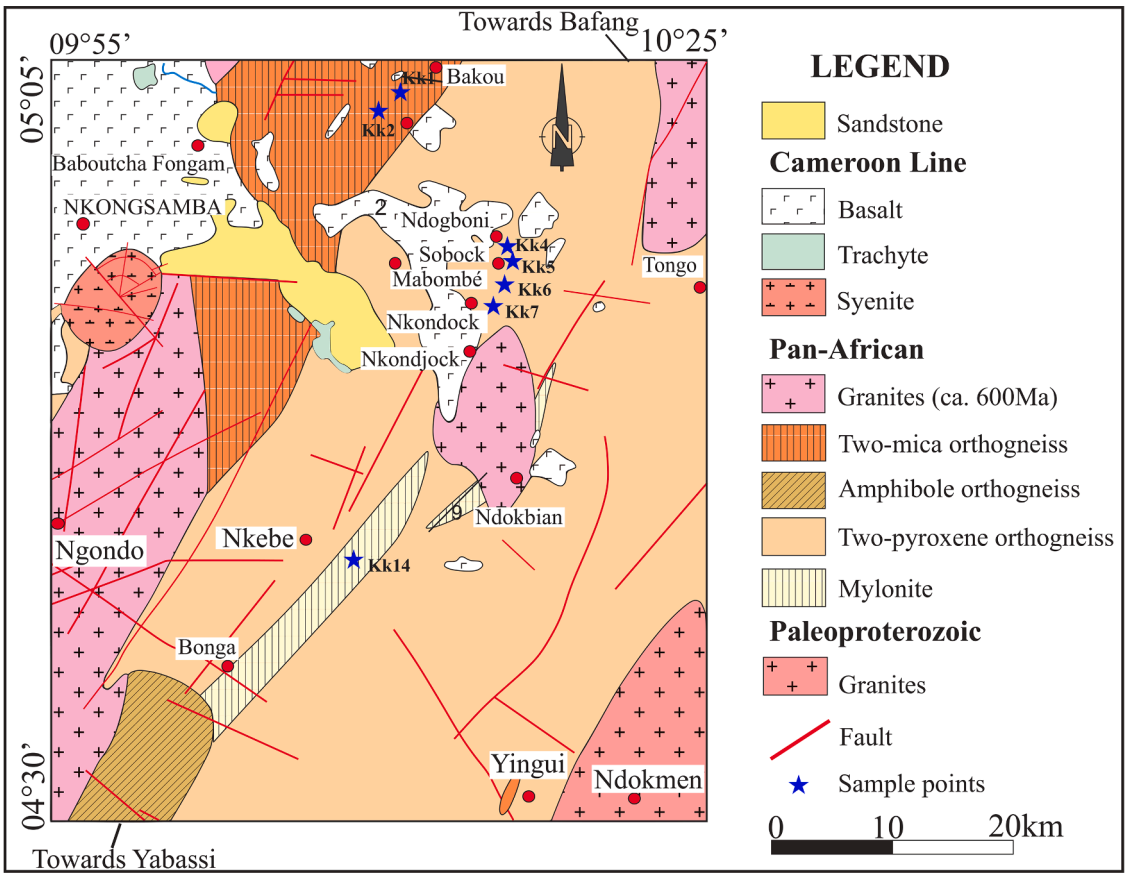

Fig. 2. Geological map of the Nkondjock region, Modified after (Dumort, 1968).

Congo craton in Cameroon. The present work is focused on Pan-African orthogneisses in the Nkondjock area located at the northwestern edge of the corridor (Fig. 1b) presumed to be located into Archean/Proterozoic suture corridor poorly known until now. Our objectives are threefold: (1) to distinguish the different rock type base on their petrographic characteristics, (2) to decipher the protoliths and petrogenesis of the orthogneisses and the timing of the magmatic and metamorphic event in the region via whole-rock major and trace element geochemistry, Sr-Nd isotopic geochemistry, and zircon U-Pb dating and Lu-Hf isotopes systematics and (3) to propose a geodynamic model for the evolution of the Pan-African belt in West Cameroon during the late-Neoproterozoic era.

2. Geological setting

The Precambrian terrains of Cameroon form the basement of the country and are composed of two petrological tectonic units (Fig. 1b): 1) the Ntem group (NT) to the south that includes the Archean (Ntem, Ayna and Nyong units) and Paleoproterozoic units (Li et al., 2007; Shang et al., 2004) and 2) the Pan-African North Equatorial Fold Belt (PANEFB) (Nzenti et al., 2011) reworked or formed during the Pan-African orogeny. Neoproterozoic Fold Belt of Cameroon (NFBC) which is part of the PANEFB was formed by convergence and collision between the Congo-São Francisco and the West African cratons (Castaing et al., 1994; Trompette, 1997) (Fig. 1a). Also involved in the collision was probably a 'ghost' currently known as the Saharan metacraton (Abdelsalam et al., 2002; Liégeois et al., 2013). The orogenic evolution of the (NFBC) experienced several phase deformations which involved various degrees of metamorphism up to granulite facies and widespread crustal anatexis as well as magmatism (Toteu et al., 2004). Numerous chronological works were reported for various rock types of NFBC since 1970 s (Lasserre and Soba, 1976). There is a general consensus that the initial and paroxysmal phases of orogenesis during the Pan-African took place at ca. 660–580 Ma in Cameroon, with an early nappe tectonics and subsequent massive granitoid magmatism (Djouka-Fonkwé et al., 2008; Penaye et al., 2006; Toteu et al., 2001).

The Nkondjock area (Fig. 1b) located at the southwestern part of the PANEFB is contiguous to sedimentary deposits linked to the West-Gondwana break-up. The area was strongly affected by thrusting and transcurrent tectonics (Njiekak et al., 2008) that led to the development of strike-slip shear zones trending mostly N-S to ENE-WSW along a corridor known as Adamawa Shear Zone (ASZ).

The ASZ basement of Paleoproterozoic and Neoproterozoic high-grade metamorphic rocks is intruded by plutonic rocks (Kamga et al., 1999; Kwékam et al., 2013; Tchaptchet Tchato, 2011). The Paleoproterozoic rocks consist of amphibole-biotite- and/or garnet-bearing pyroxene gneisses which were metamorphosed under amphibolite and up to granulite-facies conditions at 2050 Ma (Penaye et al., 2004; Toteu et al., 2001). The protolith of the Neoproterozoic rocks (garnet-biotite gneiss, sillimanite bearing garnet-biotite gneiss) were deposited in a Neoproterozoic extensional setting, (Tchaptchet Tchato, 2011) and were recrystallized at high temperature amphibolite-facies metamorphism at 580–570 Ma (EMP dating on monazite, (Tchaptchet et al., 2009) or 600 Ma (zircon U-Pb dating, following continental collision (Tchaptchet et al., 2009). The orogenic evolution of the NFBC involved polyphase deformations associated to collisional and post-collisional evolution in Cameroon domain, including various degrees of metamorphism up to granulite facies and widespread crustal anatexis and magmatism (Toteu et al., 2004). An improved geochronological framework has been proposed for the new evolution of the NFBC, i.e. >620 Ma, ca.620–600 Ma, ca. 590–580 Ma and ca.580–560 Ma for D_1, D_2, D_3 and D_4 phases of tectonic, metamorphic and magmatic events, respectively. The metamorphic rocks were overprinted by 560–552 Ma strike slip shear zone

Fig. 3. (a) Hand sample of two-mica orthogneisses showing a blurred foliation. Outcrop and hand samples of Two-pyroxene orthogneisses. (b) Outcrop in the shape of boulder showing onion-pell shape cracks. (c)Hand samples showing light grey color. (d) Hand sample and microphotographs of mylonitic orthogneisses.

(Tcheumenak Kouémo et al., 2014) which represents the SW prolongation of the Foutoni shear zone. The intrusive complexes consist of 580–547 Ma post-collisional intermediate to basic rocks (monzonite, monzogabbro, norite, gabbro) with high-K calk-alkaline to shoshonitic affinities (Kwékam et al., 2013; Ngo Belnoun et al., 2013), emplaced into late D_2 to D_3 transcurrent tectonic units (Tchaptchet Tchato, 2011) or D_4 dextral shearing zone along the CCSZ (Kwékam et al., 2013). These intrusive rocks were originated from crustal melting with little input from the mantle. The metamorphic and plutonic rocks of the Nkondjock area were partially covered by Cameroon Volcanic Line alkaline basalts dated between 10 and 6 Ma (Tchuimegnie Ngongang et al., 2015).

3. Petrography and sampling

Based on mineralogy, the studied rocks were classified as: two-mica, two-pyroxene, and mylonitic orthogneisses. In total, seven representatives outcrop sites with fresh rock from Nkondjock area in West Cameroon (Fig. 2) were examined.

Two-mica orthogneisses are found at the northern part of Nkondjock area (Fig. 2). They crop out in the form of large boulders and blocks whose sizes ranges from ten of centimeters to meters. The rocks are grey in color and slightly foliated (Fig. 3a). They mainly display heterogranoblastic texture (Fig. 4a) but are mylonitized at some places. They are composed of quartz (25%), microcline (37%) plagioclases (15%) are sometimes disturbed by microflake inclusions of micas, elongated biotite (13%) (Fig. 4b), muscovite (3%) and opaque minerals (5%) sandwiched between quartz and feldspars as well as minor secondary chlorite and sericite.

Two-pyroxene orthogneisses are found at the northeast of Nkondjock towards south of Sobock (Fig. 2). Rock outcrop present boulders and vary from dark grey to light grey in color and exhibit poorly developed foliations. Their size can reach several meters. At certain places, the rocks are weathered, cracked or broken into onion pell-like shape (Fig. 3b). They show granoblastic (Fig. 4c) to granolepidoblastic texture and are made up of quartz (15–25%), alkali feldspars represented by orthoclase (5–10%) and microcline (10 to 20%). They show myrmekite and fine lamellae perthites and some of them are weathered and partially transformed. Plagioclase (25–40%) is mostly cloudy and present growths of fine flakes of white micas with few crystals showing bent twinning (Fig. 4d). Biotite (16–25%) consists of subhedral to anhedral micro to megaflakes, and larger flakes are often skeleton-like, bent (Fig. 4d) and/or poikilitic. Clinopyroxenes (1–5%) and orthopyroxenes (3%) are subhedral to anhedral micro to phenoblasts molded between quartz, feldspars and biotite (Fig. 4f). Orthopyroxenes are not common in all samples and they are generally weathered (uralitization) (Fig. 4g) and joint to biotite and amphibole. Accessory minerals (2–5%) are zircon, apatite, opaque oxides and titanite.

Mylonitic orthogneisses are found at the south west of Nkondjock in

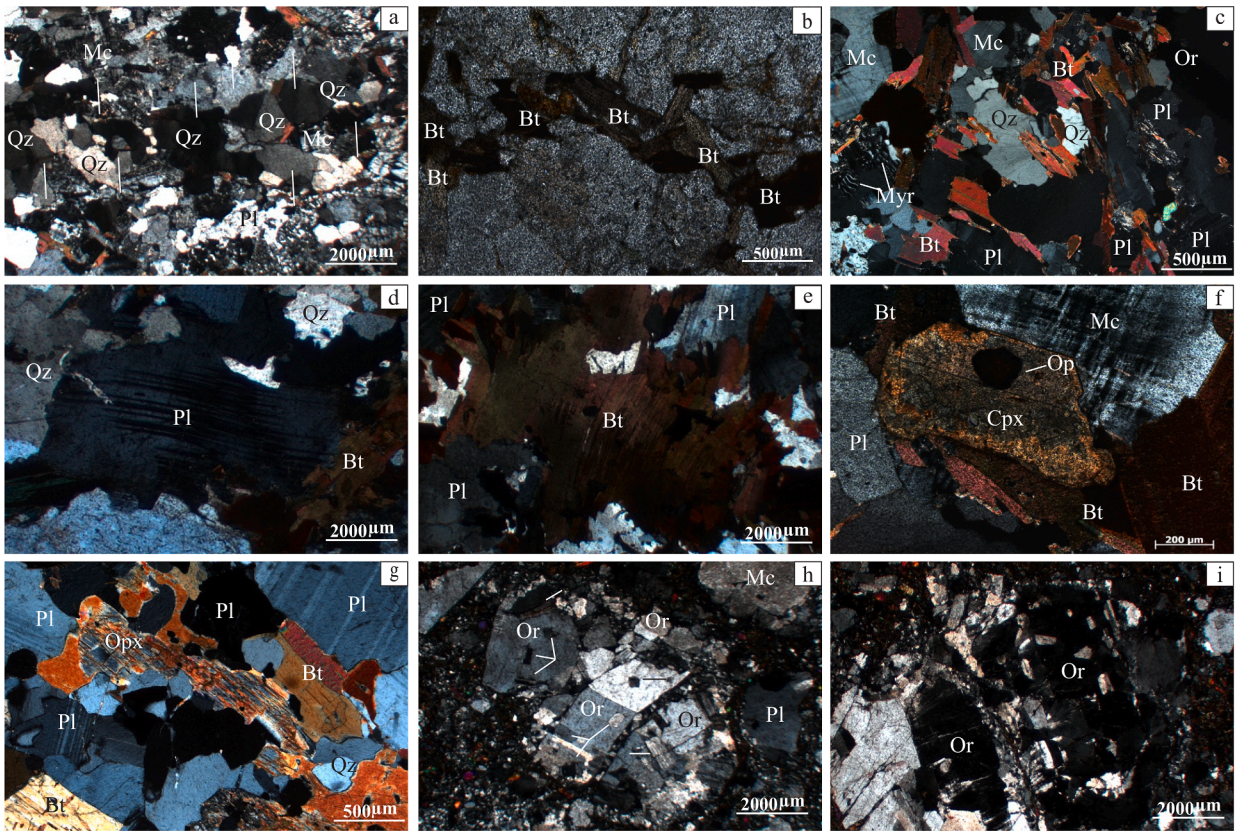

Fig. 4. (a) Microphotographs showing heterogranoblastic texture. White arrows present a monomineral layer of quartz. (b) Discontinuous microbed of biotite sandwiched among quartz and feldspars. (c) Granoblastic texture. (d) Deformed plagioclase showing bent twinning. (e) large and bent flake of biotite with numerous opaque inclusions. (f) Subhedral phenoblast of clinopyroxene showing Carlsbad twinning. (g) weathered skeleton-like orthopyroxene. (h) porphyrogranoblastic texture with a cataclastic tendency. (i) Euhedral perthites developed in orthoclase megaclasts.

the mylonitic corridor-oriented NE-SW (Fig. 2). The rocks appear in boulder shape and vary from pink to red color and are massive in structure (Fig. 3d). Their texture is granoblastic with a cataclastic mylonitic tendency (Fig. 4h, i) and they consist of quartz (10%), feldspars often cracked and bordered with subgrains of the same nature and/or subgrains of quartz (Fig. 4i). Orthoclase and microcline occupy successively about 30% and 15% of the total volume of the rock bearing numerous inclusions, fine lamellae and euhedral perthites (Fig. 4h) and plagioclase (10%). Green hornblende (13%), clinopyroxene (8%) and orthopyroxene (2%) are subrounded and subhedral microblasts gathered in polymineral assemblages (green hornblende and pyroxenes) in the spaces between pheno- and megaclasts or at times merged with quartz and feldspar microblasts in the matrix. Biotite (5%) is chloritized and commonly associated to green amphibole. Opaque oxides (3%) are associated with Fe-Mg minerals; they seem to result from the latter by alteration.

4. Analytical methods

4.1. Zircon U-Pb dating and Hf analyses

One sample from each of the three gneisses was selected for zircon U-Pb dating and Lu-Hf isotope analysis. The zircon U-Pb data are summarized in Table 1 and the representative cathodoluminescence (CL) images of the zircons are presented in (Fig. 5).

Zircon grains were separated from crushed rocks using conventional heavy liquid and magnetic techniques. Representative zircon was handpicked and mounted in epoxy resin disc, polished and photographed in transmitted and reflected light to identify grains for analysis. Cathodoluminescence (CL) images were photographed by Gatan Mono CL4 coupled with Zeiss Sigma 300 Scanning Electronic Microscope at the State Key Laboratory of Geological Process and Mineral Resource (SKLGPMR), China University of Geosciences, Wuhan. In situ U-Pb dating w**as** carried out using a 7500a Agilent ICP-MS equipped with a 193-nm ArF excimer laser ablation system in SKLGPMR. Analyses were conducted with a beam diameter of 32um, 5 Hz repetition rate for 45 s. Helium was applied as a carrier gas to allow efficient transportation of aerosol to the ICP − MS. Detailed conditions and data reduction procedures are given in (Liu et al., 2010). Zircon 91,500 was used as a primary standard in order to correct mass discrimination and elemental fractionation for U-Th-Pb. GEMOC GJ-1 was determined as unknown samples to evaluate the data quality of analysis. The obtained mean 206Pb/238U ages for GJ-1 is 599.50 ± 2.0 Ma (2σ, MSWD = 0.61, n = 12, Table S1) is consistent with the recommended value of 599.8 ± 1.7 Ma(2σ) by Jackson et al. (2004). Data calculations of U-Pb ages were made using ISOPLOT (Ludwig, 2003).

Lu-Hf isotope analyses where carried out using a Neptune plus MC-ICP-MS with a 193 nm ArF-excimer laser ablation system at SKLGPMR. Lu-Hf isotopic studies were done on the same zircon crystals that were dated by U-Pb system. All data were obtained on zircon grains in single spot ablations using a spot size of 44 μm. Zircon standard 91,500 was used for quality control. GJ-1 was analyzed as unknown samples during the analyses to evaluate the reliability of the analytical data. Detailed operating conditions for the laser ablation method and the MC-ICPMS instrument can be found in (Liu et al., 2010). The $\varepsilon_{Hf(t)}$, T_{DM1}, T_{DM2} and $f_{Lu/Hf}$, the ^{176}Lu decay constant of 1.867×10^{-11} $year^{-1}$, $^{176}Hf/^{177}Hf_{CHUR}$ = 0.282772, $^{176}Lu/^{177}Hf_{CHUR}$ = 0.0332, $^{176}Lu/^{177}Hf_{DM}$ = 0.233251, and $^{176}Lu/^{177}Hf_{DM}$ = 0.0384 for the Chondrite Uniform Reservoir (CHUR) and Depleted Mantle (DM) (Blichert-Toft and Albarède, 1997; Griffin et al., 2000).

Table 1
LA-ICP-MS zircon U-Pb data of gneissic rocks from Nkondjock.

Spot	Th	U	$^{207}Pb/^{206}Pb$		$^{207}Pb/^{235}U$		$^{206}Pb/^{238}U$		Th/U	$^{207}Pb/^{206}Pb$		$^{207}Pb/^{235}U$		$^{206}Pb/^{238}U$		Con. (%)
	ppm	ppm	Ratio	1σ	Ratio	1σ	Ratio	1σ		Age(Ma)	1σ	Age(Ma)	1σ	Age(Ma)	1σ	
Sample KK1-01, two-micas gneisses from Nkondjock, N.05°04′35.2″ E.10°10′53.7″																
1	51	84	0.06	0.002	0.839	0.023	0.1006	0.0013	0.61	587	38	619	13	626	8	99.2
2	127	150	0.06	0.002	0.837	0.022	0.0992	0.0013	0.84	611	35	617	12	620	7	99.2
3	114	147	0.06	0.002	0.833	0.023	0.0996	0.0012	0.77	598	39	615	13	619	7	96.3
4	149	200	0.059	0.002	0.825	0.024	0.0994	0.0012	0.74	561	44	611	13	621	7	99.5
5	103	118	0.062	0.002	0.876	0.028	0.1020	0.0012	0.88	672	47	639	15	629	7	99.9
6	106	132	0.056	0.002	0.789	0.028	0.1016	0.0013	0.81	456	56	591	16	626	7	88.8
7	117	168	0.059	0.002	0.835	0.03	0.1015	0.0012	0.69	550	58	616	17	633	7	99.6
8	161	221	0.058	0.002	0.823	0.031	0.1002	0.0011	0.73	539	62	610	17	627	7	###
9	117	165	0.058	0.002	0.827	0.032	0.1026	0.0012	0.71	528	63	612	18	632	7	###
10	161	191	0.058	0.002	0.817	0.03	0.1036	0.0020	0.84	528	56	607	17	626	8	###
11	140	166	0.058	0.002	0.797	0.028	0.1024	0.0012	0.84	509	50	595	16	616	9	99.7
12	172	210	0.058	0.002	0.813	0.024	0.1016	0.0010	0.82	522	45	604	13	627	6	99.4
13	137	149	0.06	0.002	0.835	0.024	0.0998	0.0010	0.92	606	44	616	13	617	6	95.0
14	127	168	0.059	0.002	0.837	0.022	0.1032	0.0012	0.75	572	37	618	12	629	7	99.5
15	78	126	0.058	0.002	0.799	0.022	0.1006	0.0011	0.62	528	41	596	13	617	7	92.3
16	84	131	0.059	0.001	0.835	0.022	0.1025	0.0012	0.64	576	35	617	12	627	7	99.9
Sample KK4-01, two-pyroxenes gneisses from Nkondjock, N.04°56′22.9″ E.10°16′09.0″																
1	68	62	0.06	0.002	0.807	0.028	0.0961	0.0017	1.1	611	45	601	16	603	10	99%
2	81	72	0.059	0.002	0.801	0.029	0.0967	0.0015	1.11	576	49	598	16	602	10	99%
3	47	57	0.06	0.002	0.804	0.029	0.0952	0.0017	0.82	611	53	599	16	600	9	99%
4	109	81	0.06	0.002	0.78	0.022	0.0941	0.0015	1.34	587	37	585	13	585	8	99%
5	60	58	0.06	0.002	0.807	0.026	0.1001	0.0018	1.02	617	40	601	15	601	10	99%
6	74	63	0.061	0.002	0.813	0.028	0.0987	0.0022	1.18	628	39	604	16	603	13	99%
7	49	54	0.06	0.002	0.828	0.034	0.0954	0.0016	0.9	609	56	612	19	613	11	99%
8	42	44	0.061	0.003	0.837	0.034	0.0980	0.0019	0.95	620	52	618	19	621	12	99%
9	87	75	0.06	0.002	0.826	0.03	0.0988	0.0017	1.15	606	51	611	17	611	9	99%
10	126	97	0.061	0.002	0.843	0.026	0.0972	0.0018	1.29	643	37	621	14	614	10	98%
11	92	71	0.057	0.002	0.773	0.022	0.0981	0.0018	1.29	500	31	581	12	608	11	95%
12	112	90	0.058	0.002	0.8	0.025	0.0943	0.0015	1.25	524	41	597	14	617	10	96%
13	90	95	0.06	0.002	0.823	0.023	0.1007	0.0016	0.94	598	32	610	13	614	10	99%
14	77	76	0.06	0.002	0.813	0.025	0.0981	0.0014	1.01	587	42	604	14	609	9	99%
15	111	91	0.061	0.002	0.824	0.025	0.0921	0.0014	1.22	620	37	610	14	609	10	99%
16	81	69	0.067	0.002	0.934	0.03	0.0945	0.0016	1.18	848	41	670	16	617	9	91%
Sample KK14-01 mylonitic gneisses from Nkondjock, N.04°41′58.9″ E.10°08′46.5″																
1	1693	750	0.065	0.002	1.041	0.027	0.1232	0.0028	0.7	789	26	724	14	717	13	98%
2	2042	844	0.064	0.002	0.868	0.029	0.1010	0.0016	1.6	724	44	635	16	610	9	96%
3	219	640	0.061	9E-04	0.861	0.015	0.1095	0.0014	0.5	620	18	631	8	635	8	99%
4	2173	1402	0.125	0.001	6.424	0.109	0.3967	0.0056	1	2035	13	2036	15	2036	25	99%
5	61.8	71.5	0.064	0.002	1.007	0.027	0.1178	0.0022	0.9	752	27	707	14	705	14	99%
6	188	199	0.062	0.001	0.863	0.015	0.1107	0.0012	0.9	680	17	632	8	624	10	98%
7	81	207	0.13	0.001	6.725	0.09	0.3793	0.0054	0.4	2099	11	2076	12	2051	19	98%
8	113	74.8	0.062	0.002	0.839	0.022	0.1024	0.0017	1.5	661	31	618	12	609	9	98%
9	111	75	0.061	0.002	0.838	0.024	0.1058	0.0015	1.5	632	36	618	13	617	9	99%
10	142	145	0.063	0.001	1.003	0.02	0.1193	0.0014	1	709	22	706	10	705	8	99%
11	114	243	0.128	0.004	6.382	0.094	0.4016	0.0034	0.5	2069	15	2030	13	2031	33	99%
12	34.3	41.7	0.064	0.003	1.002	0.039	0.1141	0.0024	0.8	731	46	705	20	706	15	99%
13	57.6	54.8	0.06	0.002	0.969	0.034	0.1168	0.0021	1.1	594	48	688	17	719	11	95%
14	40.5	44.4	0.064	0.002	0.907	0.033	0.1110	0.0014	0.9	744	49	656	18	633	10	96%
15	116	140	0.061	0.001	0.991	0.02	0.1213	0.0013	0.8	656	25	699	10	716	7	97%
16	144	219	0.063	0.001	0.871	0.016	0.1065	0.0012	0.7	696	20	636	9	620	8	97%

Note: [a] Degree of concordance = 100*($^{206}Pb/^{238}U$ age)/($^{207}Pb/^{235}U$ age).

4.2. Major and trace elements analysis

Major element analyses were performed using X-ray fluorescence (XRF) on fused glasses at SKLGPMR. Visibly fresh pieces of rock (~20 g) were crushed to 200-mesh in an alloy mortar. Loss on Ignition (LOI) values were determined on 1 g sample powder after heating it to 1000°C for 90 min. Analyses of international rock standards (BCR-2, GSR-1 and GSR-3) demonstrate precision and accuracy better than 5% for major oxides.

Trace elements were analyzed on an Elan DRC-II ICP-MS in University of Science and Technology of Hefei, China. 50 ± 1 mg of sample powder was digested in HF + HNO_3 mixing in a Teflon bomb which is sealed and heated to 190 °C for 48 h. The clear sample solution was mixed with Rh solution as an internal standard. Pure elemental standards were used for external calibration and BHVO-2, AGV-2 and BCR-2 were used as reference materials. The analytical precision is better than 5% for elements with concentrations > 10 ppm, and better than 10% for those with concentration <10 ppm concentration.

4.3. Sr-Nd isotopic analysis

For whole rock Sr-Nd isotopic analysis, ~ 100 mg sample powder was dissolved in distilled HF + HNO_3 in Teflon capsules which is sealed and heated to 190 °C for 48 h, and elemental separation was done by conventional cation-exchange techniques (Chen et al., 2007, 2009). The Sr-Nd isotopes were acquired without doing isotope dilution. The $^{87}Rb/^{86}Sr$ and $^{147}Sm/^{144}Nd$ are calculated from trace element data for a different aliquot of the same powder. Sr and Nd were separated and purified on quartz columns by conventional ion exchange chromatography with a 5-ml resin bed of AG 50 W-X12 (200–400 mesh) and

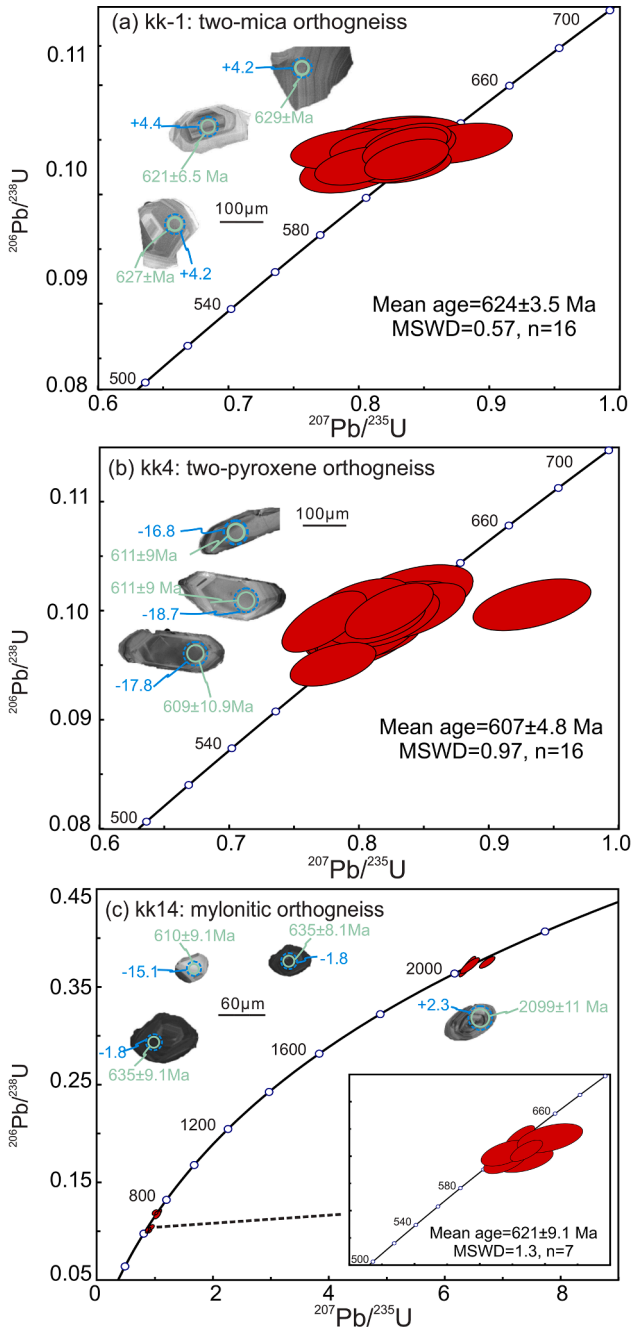

Fig. 5. Cathodoluminescence images of zircon from Nkondjock orthogneisses, circle and number indicate the locations of spot analyses and associated ages, with $^{206}Pb/^{238}U$ ages shown as green circle and the bigger blue circles show the locations of Hf isotope analyses and corresponding to εHf (t) values and Concordia plot of zircons for two-mica, two-pyroxene and mylonitic orthogneisses from Nkondjock area. (For interpretation of the references to color in this figure legend, the reader is referred to the web version of this article.)

HDEHP, di (2-ethylhexyl) orthophosphoric acid after sample dissolution. All isotopic measurements were made on a Finnigan MAT-262 mass spectrometer at University of Science and Technology of Hefei, China. Sr was loaded with a Ta-HF activator on preconditioned W filaments and was measured in single-filament mode. Nd was loaded as phosphate on preconditioned Re filaments and measurements were performed in a Re double filament configuration. $^{87}Sr/^{86}Sr$ ratios were normalized to $^{86}Sr/^{88}Sr = 0.1194$ and $^{143}Nd/^{144}Nd$ ratios to $^{146}Nd/^{144}Nd = 0.7219$. The decay constants (λ) used were 1.42×10^{-11} for ^{87}Rb and 6.54×10^{-12} for ^{147}Sm. εNd(t) value were calculated on the basis of the following present-day reference values for the chondritic uniform reservoir $(^{143}Nd/^{144}Nd)_{CHUR} = 0.512630 \pm 11$ and $(^{147}Sm/^{144}Nd)_{CHUR} = 0.1960 \pm 4$.

5. Results

5.1. Zircon U-Pb dating and Lu-Hf isotopes

Zircon U-Pb and Lu-Hf analytical dataset of two-mica, two-pyroxene and mylonitic orthogneisses from Nkondjock area are listed in Tables 1 and 2 and representative CL images are shown in Fig. 5.

5.1.1. Two mica orthogneisses

Zircon grains from two-mica orthogneiss (sample kk1) are generally euhedral to subhedral and show core-rim structures. The core show significantly strong to weak oscillatory zoning in CL images with high Th/U ratios (0.61–0.72) (Fig. 5a; Table 1), indicative of a magmatic origin. Sixteen analyses of zircon core grains are concordant with $^{206}Pb/^{238}U$ ages ranging from 617 ± 6.2 to 633 ± 6.8 Ma, yielding a weighted mean age of 624 ± 3.5 Ma (MSWD = 0.57), which is interpreted as the time of crystallization of the protolith (Fig. 5a).

Magmatic zircon grains from this sample have initial $^{176}Hf/^{177}Hf$ ratio of 0.282470–0.282524 and εHf(t) value ranging from +3 to +4.9 (Table 2), with a weighted average εHf(t) value of +3.7 ± 0.4. The calculated T_{DM2} model age ranges from 1208 to 1316 Ma, respectively (Table 2).

5.1.2. Two-pyroxene orthogneisses

Most zircon grains from two-pyroxene orthogneisses (sample kk4) are euhedral to subhedral. They are characterized by well-developed oscillatory zoning with visible core-rim structures. Zircon cores have moderate Th/U (0.82–1.34) (Fig. 5b; Table 1), indicating a magmatic origin. Sixteen zircon grains have $^{206}Pb/^{238}U$ ages ranging from 585 ± 7.8 to 621 ± 12.1 Ma with a weighted mean age of 607 ± 4.8 Ma (MSWD = 0.97), which is interpreted as the crystallization age of the protolith of the two-pyroxene gneisses (Fig. 5b).

Magmatic zircon grains from this sample have initial $^{176}Hf/^{177}Hf$ ratio of 0.281856–0.281932 and εHf(t) value ranging from −19.1 to −16.4 (Table 2), with a weighted average εHf(t) value of − 18.2 ± 0.4. The calculated T_{DM2} model age ranges from 2321 to 2461 Ma.

5.1.3. Mylonitic orthogneisses

Zircon grains separated from mylonitic sample kk14 are mostly euhedral to subrounded with fine oscillatory core, typical of zircon grains crystallized from magmas with high Th/U ratios (0.5–3.0) (Fig. 5c; Table 1), which also confirm their magmatic origin. Seven out of sixteen zircon grains display $^{206}Pb/^{238}U$ ages ranging from 609 ± 9.2 to 635 ± 8.1 Ma yielding a weighted mean age of 621.3 ± 9.1 Ma (MSWD = 1.3) can be considered as the crystallization age of the protolith for mylonitic orthogneisses. Nine other analyses yield large age variation ranging from 705 ± 8.4 to 2099 ± 11 Ma, which are obviously older than crystallization age (Fig. 5c). The latter were probably inherited from the source region and/or introduced from the wall rocks (Table 1).

Magmatic zircon grains have initial $^{176}Hf/^{177}Hf$ ratio of 0.281954–0.282324 and εHf(t) value ranging from −15.6 to −2.1 (Table 2), with a weighted average εHf(t) value of 10.1 ± 0.5. The calculated T_{DM2} model age ranges from 1584 to 2280 Ma. Four other analyses with age that range from 705 ± 8 to 717 ± 11 Ma have initial $^{176}Hf/^{177}Hf$ ratio of 0.282337–0.282398 and εHf(t) value ranging from −0.1 to +2.1. The calculated T_{DM2} model age ranges from 1416 to 1531 Ma. Three analysis yield ages ranging from 2035 ± 13 to 2099 ± 11 Ma have initial $^{176}Hf/^{177}Hf$ ratio of 0.281162–0.281509 and εHf(t) value ranging from −10.7 to +2.4. The calculated T_{DM2} model age ranges from 2505 to 3172 Ma. Some zircon grains (kk14-01–1,3, 4, 5, 6, 7, 10, 12) with $^{176}Lu/^{177}Hf$ ratio of ≥0.0005 indicate that they cannot represent

Table 2
LA-MC-ICP-MS Hf isotopic compositions of zircons from Nkondjock gneisses.

Spot	Age (Ma)	$^{176}Yb/^{177}Hf$	1σ	$^{176}Lu/^{177}Hf$	1σ	$^{176}Hf/^{177}Hf$	1σ	$^{176}Hf/^{177}Hf_i$	εHf(t)[a]	±1σ	T_{DM2} (Ma)[b]
KK1-01, two-micas gneiss											
1	624	0.006168	0.000063	0.00017	0.000002	0.28248	0.00001	0.282474	3.0	0.4	1305
2	624	0.010830	0.000131	0.00029	0.000002	0.28249	0.00001	0.282483	3.1	0.4	1291
3	624	0.010707	0.000105	0.00029	0.000002	0.28247	0.00001	0.282470	2.7	0.4	1316
4	624	0.014570	0.000153	0.0004	0.000001	0.28251	0.00001	0.282507	4.0	0.4	1244
5	624	0.011800	0.000096	0.00031	0.000001	0.2825	0.000009	0.282499	3.9	0.3	1256
6	624	0.012539	0.000104	0.00034	0.000001	0.28249	0.000013	0.282489	3.5	0.5	1277
7	624	0.015292	0.000130	0.00042	0.000001	0.28253	0.000011	0.282524	4.9	0.4	1208
8	624	0.019883	0.000143	0.00054	0.000001	0.28252	0.00001	0.282518	4.5	0.4	1222
9	624	0.016653	0.000090	0.00046	0.000004	0.28251	0.000008	0.282507	4.3	0.3	1241
10	624	0.015173	0.000096	0.0004	0.000001	0.28248	0.000009	0.282478	3.1	0.3	1297
11	624	0.013051	0.000089	0.00036	0.000001	0.2825	0.00001	0.282495	3.5	0.4	1270
12	624	0.007144	0.000092	0.00018	0.000001	0.2825	0.00001	0.282501	3.9	0.4	1254
KK4-01 two-pyroxene gneiss											
1	607	0.008922	0.000086	0.00022	0.000002	0.28187	0.000011	0.281866	−19.1	0.4	2450
2	607	0.013509	0.000291	0.00033	0.000005	0.28189	0.000012	0.281890	−18.2	0.4	2404
3	607	0.010857	0.000120	0.00026	0.000005	0.28189	0.000012	0.281883	−18.5	0.4	2418
4	607	0.013564	0.000267	0.00033	0.000004	0.2819	0.000011	0.281896	−18.4	0.4	2399
5	607	0.008609	0.000268	0.00021	0.000004	0.28188	0.000011	0.281878	−18.7	0.4	2428
6	607	0.012656	0.000289	0.0003	0.000005	0.28187	0.000011	0.281864	−19.2	0.4	2453
7	607	0.009298	0.000216	0.00022	0.000004	0.28189	0.000011	0.281883	−18.2	0.4	2413
8	607	0.008014	0.000144	0.0002	0.000002	0.28186	0.000013	0.281856	−19.0	0.5	2461
9	607	0.019929	0.000637	0.00047	0.000015	0.28192	0.000014	0.281918	−17.1	0.5	2350
10	607	0.014232	0.000163	0.00034	0.000005	0.28192	0.00001	0.281920	−16.9	0.4	2345
11	607	0.009331	0.000191	0.00023	0.000003	0.28189	0.000011	0.281890	−18.1	0.4	2402
12	607	0.017926	0.000341	0.00042	0.000003	0.28194	0.000011	0.281932	−16.4	0.4	2321
KK14-01 mylonitic gneiss											
1	621	0.021833	0.000582	0.0006	0.000007	0.282347	0.000013	0.282339	0.2	0.5	1523
2	621	0.013362	0.000352	0.00032	0.000009	0.281970	0.000014	0.281966	−15.4	0.5	2261
3	621	0.065863	0.001570	0.00215	0.000042	0.282349	0.000018	0.282324	−2.1	0.6	1584
4	2035	0.017740	0.000482	0.0005	0.00001	0.281475	0.000023	0.281456	−1.0	0.8	2634
5	621	0.023641	0.000353	0.00069	0.000007	0.282401	0.000013	0.282392	1.8	0.5	1428
6	621	0.018571	0.000245	0.00047	0.000005	0.282328	0.000012	0.282322	−2.4	0.4	1591
7	2099	0.031821	0.001298	0.0008	0.000024	0.281541	0.000012	0.281509	2.4	0.4	2505
8	621	0.008384	0.000255	0.0002	0.000003	0.281976	0.000012	0.281973	−15.1	0.4	2248
9	621	0.007885	0.000094	0.00019	0.000002	0.281957	0.000011	0.281954	−15.6	0.4	2280
10	621	0.021505	0.000230	0.00055	0.000005	0.282344	0.000012	0.282337	−0.1	0.4	1531
11	2069	0.014967	0.000148	0.00038	0.000004	0.281177	0.000012	0.281162	−10.7	0.4	3172
12	621	0.018579	0.000255	0.0005	0.000006	0.282405	0.000012	0.282398	2.1	0.4	1416

a: εHf(t) values are calculated using the $^{207}Pb/^{206}Pb$ age determined by LA-ICP-MS dating. $^{176}Hf/^{177}HfCHUR = 0.282772$. (Blichert-Toft and Albarède, 1997).
b: Two stage model age in Billion years (Ga) are calculated using the measured $^{176}Lu/^{177}Hf$ of each spot, a value of 0.009 for the bulk Precambrian crust (Vervoort and Jonathan Patchett, 1996), and a depleted mantle $^{176}Lu/^{177}Hf$ and $^{176}Hf/^{177}Hf$ of 0.0384 and 0.28325, respectively (see Griffin et al., 2000 for details and references).

their initial $^{176}Hf/^{177}Hf$ composition and thus will not be considered in our discussion (Kinny and Maas, 2003).

5.2. Whole rock major and trace elements geochemistry

Whole rock major and trace elements analyses of 16 representative samples are listed in Table 3.

The two-mica orthogneisses have high SiO_2 (69.79–71.91 wt%), high total alkalis ($Na_2O + K_2O = 7.72$ to 8.69 wt%), and plot in the granitic field (Fig. 6b). They have relatively high Al_2O_3 (14.7–15.98 wt%) and low MgO (0.21–0.39 wt%) and CaO (0.26–0.67 wt%) contents (Table 3) with A/CNK value >1.1 (Fig. 6a). Two-mica orthogneisses show enrichment in light rare earth elements (LREE) (e.g. high La/Yb_N: 39.4–56.6; N stand for chondrite-normalized) and strong depletion in heavy rare earth element (HREE) (e.g. low Yb: (0.42–0.59 ppm) with negative Eu anomalies (Eu/Eu* =0.34–0.89) (Fig. 7a). In the primitive mantle-normalized multi-element spider diagrams, the two-mica orthogneisses define pronounced positive LILE and negative Nb, Ta, Ti, Y, P and Sr anomalies (Fig. 7b). They also have wide range of Sr from 77.1 to 376 ppm, Cr from 9.07 to 141 ppm, Ni from 3.73 to 20.3 ppm with wide range of Sr/Y ratios (18–101.38).

The Ndogboni two-pyroxene orthogneisses have relatively lower SiO_2 (62.4–63.27 wt%), Al_2O_3 (14.83–15.64 wt%), total alkalis ($Na_2O + K_2O = 7.84$–8.08 wt%) and plot within the quartz-monzonite field in the total alkali-silica diagram of (Middlemost, 1994) (Fig. 6b). They also contain low concentration of MgO (1.46–1.69 wt%), CaO (2.48 to 2.96 wt%) contents and Mg# (38.7–41.7) value. They have strongly fractionated REE patterns (e.g La/Yb_N ratios ranging from (52.9–98.8) and Low HREE concentrations (e.g. Yb 0.73–1.18 ppm) with negative Eu anomalies (Eu/Eu*= 0.56–0.69) (Table 3, Fig. 7c). Their primitive mantle normalized multi-element patterns show a decrease from LILE to HFSE with obviously negative Nb, Ta and Ti and positive LILE anomalies (Fig. 7d). They also display high Sr (405–447 ppm), Cr (138–143 ppm) and Ni (13.6–28.8 ppm) concentrations with high Sr/Y ratios (26.2.7–38.9). In contrast to the Ndogboni two-pyroxene orthogneisses, the Mabombé two-pyroxene orthogneisses have high SiO_2 (73.73–74.66 wt%), low Al_2O_3 (12.81–13.18 wt%) and total alkalis ($Na_2O + k_2O =$ 6.05 to 6.34 wt%) contents, plotting in the granitic field (Fig. 6b). They also show slightly weaker peraluminous character with A/CNK of 1.05–1.02 (Fig. 6a). On chondrite normalized REE patterns, they display relative enrichment of LREE with La/Yb_N ratios ranging from 29.7 to 45.2 and depletion of HREE with (Yb = 0.50–0.81) and positive Eu anomalies (Eu/Eu*=2.22–3.07) (Table 3, Fig. 7c). Their primitive mantle normalized trace-element patterns show a decrease from LILE to HFSE with negative Nb, Ta and Ti and positive Pb anomalies (Fig. 7d). They also display high Sr (292–481 ppm), Ba (1407–1764 ppm), Cr (112–123 ppm) and Ni (6.96–48.7 ppm) concentrations with high Sr/Y (71.9–82.2) ratios when compared to the rest (26.2–38.9). On the Harker diagram (Fig. 10), major elements of two-pyroxene orthogneisses decrease with an increasing of SiO_2 whereas Na_2O remain nearly

Table 3
Major and trace elemental compositions of gneisses from Nkondjock.

	Bakou		Bakambe		Ndogboni							Mabombe			Tombessala	
	KK1-01	KK1-02	KK2-02	KK2-03	KK4-01	KK4-02	KK4-03	KK4-04	KK5-01	KK5-02	KK5-03	KK6-01	KK6-03	KK6-04	KK14-01	KK14-02
	Two-mica gneisses				Two-pyroxene gneisses										Mylonitic gneisses	
Major elements (wt%)																
SiO_2	70.62	69.79	70.78	71.91	63.27	62.99	62.40	62.71	63.23	63.03	63.10	74.66	73.73	73.72	58.94	56.54
TiO_2	0.13	0.12	0.12	0.12	1.28	1.23	1.24	1.28	1.13	1.11	1.17	0.27	0.24	0.26	0.53	0.56
Al_2O_3	15.44	15.98	14.84	14.70	15.64	15.37	15.56	15.52	15.03	14.96	14.83	13.18	12.85	12.81	18.86	19.57
Fe_2O_3	0.86	0.75	1.07	1.04	5.48	5.14	5.38	5.39	5.28	5.36	5.55	1.56	1.60	1.56	3.36	3.86
MnO	0.01	0.01	0.02	0.02	0.04	0.03	0.04	0.04	0.06	0.05	0.06	0.02	0.02	0.02	0.09	0.09
MgO	0.36	0.39	0.21	0.22	1.69	1.56	1.66	1.63	1.46	1.47	1.50	0.50	0.46	0.50	1.14	1.25
CaO	0.67	0.55	0.26	0.43	2.59	2.48	2.48	2.51	2.95	2.96	2.96	2.17	2.11	2.10	3.06	3.36
Na_2O	2.35	1.84	1.55	1.81	3.21	3.15	3.10	3.31	3.15	3.13	3.11	3.42	3.43	3.27	5.01	4.76
K_2O	6.34	6.51	6.18	5.98	4.66	4.83	4.75	4.77	4.79	4.78	4.89	2.71	2.62	3.08	5.98	5.40
P_2O_5	0.11	0.10	0.03	0.04	0.54	0.52	0.53	0.52	0.46	0.47	0.48	0.04	0.04	0.04	0.28	0.29
LOI	2.05	2.96	2.89	2.39	2.68	0.74	1.25	1.53	1.06	1.29	0.85	0.48	0.72	0.56	1.35	1.81
Tol	98.9	99.0	97.9	105.6	101.1	98.0	98.4	99.2	98.6	98.6	98.4	99.0	97.8	97.9	98.6	97.5
Mg#	49.7	55.0	30.8	32.9	41.8	41.4	41.7	41.3	39.2	39.0	38.7	42.6	40.3	42.8	44.1	43.1
Trace elements (ppm)																
Li	19.5	18.6	7.04	9.35	36.5	33.7	36.5	30.7	33.4	32.9	33.3	8.61	8.32	6.83	11.7	11.2
Be	2.20	1.85	3.04	2.65	1.31	1.54	1.18	1.08	2.09	2.33	1.42	2.16	2.45	1.79	1.70	2.50
Sc	3.98	3.4	3.46	3.44	7.89	7.19	7.65	7.41	8.91	8.44	8.88	4.58	3.74	5.06	5.0	5.69
V	50.9	23.2	38.7	40.7	120	114	122	123	108	107	107	46.6	42.9	44.9	76	80.9
Cr	121	9.07	117	141	140	140	143	142	140	138	137	123	120	112	117	115
Ni	3.73	16.1	8.12	20.3	13.6	18.6	28.8	24.8	19.5	21.6	27	6.96	48.7	31	11.2	17.2
Cu	2.53	10.7	1.67	2.23	25.8	26.9	32.1	29.3	30.8	34.4	30.5	8.93	12	6.73	2.96	3.18
Zn	24.1	21.4	41.6	45.7	120	88.5	103	121	125	126	130	40.7	39.9	36.5	97.0	105
Ga	18.3	18.7	15.9	17.6	24.7	24.4	25.4	26	26.5	25.5	25	18.2	18.3	18.1	26.9	28.0
Rb	139	147	275	262	164	142	146	145	181	160	181	68.6	64.4	69.3	144	151
Sr	376	347	77.1	90.3	421	405	421	425	447	432	433	292	350	481	741	808
Y	5.67	3.43	4.29	4.12	10.8	11.2	11.2	11.3	16.5	15.9	16.5	3.88	4.26	6.69	13.4	12.6
Zr	194	100	164	156	772	506	785	799	366	519	563	190	137	209	384	409
Nb	2.4	1.77	11.5	6.79	26.0	27.3	28.5	29.4	30.9	30.5	31.3	7.54	6.37	7.08	26.6	27.6
Cs	2.54	2.58	2.12	1.94	0.89	0.84	0.88	0.82	0.79	0.77	0.79	0.49	0.43	0.44	1.12	1.25
Ba	2309	23,317	332	349	1981	1999	2104	2096	1910	1848	1905	1419	1407	1763	1180	1146
La	40.4	27.8	31.2	32.9	100	91.5	115	99.1	125	114	86.5	31.6	30.5	33.4	92.2	83.4
Ce	101	42.5	60.4	59.8	201	190	236	203	250	226	181	50.4	47.6	56.1	186	172
Pr	8.64	6.35	6.04	6.54	25.0	23.3	28.1	24.9	28.3	26.4	22.2	4.64	4.57	6.13	22.5	21.5
Nd	31.3	22.8	21.0	22.1	96.5	91.8	109	101	107	98.8	86.3	15.4	14.9	22.1	84.5	78.9
Sm	5.27	4.01	3.95	3.95	13.2	12.4	14.4	13.6	14.7	14.08	13.6	2.06	2.02	3.36	12.8	12.6
Ti	797	689	737	707	7684	7361	7457	76,721	6773	6665	6983	1606	1433	1552	3165	3375
Eu	1.09	1.03	0.40	0.50	2.59	2.45	2.67	2.69	2.5	2.51	2.33	1.82	2	2.38	1.97	1.88
Gd	4.51	3.09	3.18	3.49	10.6	9.57	11.3	10.9	12.5	12.08	11.3	1.97	1.96	3.21	10.5	9.84
Tb	0.49	0.39	0.38	0.37	1.0	0.96	1.07	1.08	1.27	1.21	1.2	0.21	0.23	0.40	1.06	0.98
Dy	2.13	1.49	1.6	1.49	3.75	3.78	4.32	4.16	5.46	5.28	5.26	0.93	1.1	1.81	4.25	3.86
Ho	0.28	0.23	0.18	0.19	0.46	0.45	0.46	0.46	0.69	0.66	0.68	0.17	0.18	0.3	0.51	0.49
Er	0.81	0.58	0.58	0.61	1.41	1.58	1.56	1.49	2.07	2.09	2.04	0.51	0.58	0.93	1.66	1.51
Tm	0.09	0.10	0.08	0.07	0.12	0.16	0.13	0.12	0.19	0.19	0.20	0.08	0.08	0.13	0.17	0.17
Yb	0.59	0.51	0.50	0.42	0.73	1.02	0.83	0.88	1.18	1.16	1.17	0.50	0.55	0.81	1.23	1.12
Lu	0.10	0.10	0.08	0.08	0.11	0.14	0.12	0.14	0.16	0.16	0.18	0.07	0.1	0.15	0.18	0.18
Hf	4.89	4.91	6.37	6.63	17.7	13.1	20.3	19.9	10.4	13.8	15	4.79	8.99	9.57	10.7	12.0
Ta	0.13	0.51	0.94	0.56	0.61	0.98	1.18	1.11	1.4	1.27	1.51	0.37	1.39	1.03	1.34	1.48
Pb	40.7	42.4	45.6	49.9	18.0	18.2	19.1	18.9	20.6	20.4	20.6	16.1	15.7	17.4	45.2	45.5
Th	13.2	8.82	51.2	49.4	19.8	14.8	21.6	16.9	20.2	18.1	13.2	8.82	8.47	11.4	49.5	53.2
U	2.53	1.79	4.7	4.17	0.39	0.47	0.46	0.44	0.56	0.56	0.61	0.75	0.68	1.51	5.05	5.14
Eu/Eu*	0.69	0.89	0.34	0.41	0.67	0.69	0.64	0.68	0.56	0.59	0.58	2.76	3.07	2.22	0.52	0.52
Sr/Y	66.3	101.4	18.0	21.9	38.9	36.3	37.7	37.5	27.1	27.2	26.2	75.3	82.2	71.9	55.4	64.0
A/CNK (molar)	1.29	1.44	1.53	1.44	1.04	1.03	1.06	1.02	0.96	0.95	0.94	1.05	1.04	1.02	0.93	0.99
$(La/Yb)_N$	48.9	39.4	44.8	55.6	98.7	64.3	98.8	81.2	76.1	70.9	52.9	45.2	39.9	29.7	53.6	53.4

Note: Fe_2O_3T, total iron as Fe_2O_3; LOI: loss on ignition; Mg#=molar $100*Mg^{2+}/(Mg^{2+}+Fe^{2+})$, assume Fe^{2+}/Total Fe = 0.85, A/CNK molar = $Al_2O_3/(CaO + Na_2O + K_2O)$; Subscript N = chondrite-normalized value from Sun and McDonough (1989).

constant.

Mylonitic orthogneisses contain SiO_2 concentrations of 56.5 to 58.9 wt%, high total alkali concentrations ($Na_2O + K_2O$ = 10.2–11.0 wt%) and are classified as monzonite to quartz monzonite in the total alkali-silica diagram of (Middlemost, 1994) (Fig. 6b). They have relatively low MgO (1.14–1.25 wt%) and CaO (3.06–3.36 wt%). Mylonitic orthogneisses show LREE-enriched and HREE-depleted chondrite-normalized REE patterns with La/Yb_N values of 53.4–53.6 and negative Eu anomalies (Eu/Eu*=0.52) (Table3; Fig. 7e). In the primitive mantle-normalized multi-element patterns, they show enrichment in LILE (Pb, Rb) and depletion in Nb, Ta and Ti (Fig. 7f). They also display high Sr (742–807.68 ppm), Ba (1146–1180 ppm), Cr (115–117.07 ppm) and Ni (11.2–17.20 ppm) concentrations with high Sr/Y ratios (55.4–53.6).

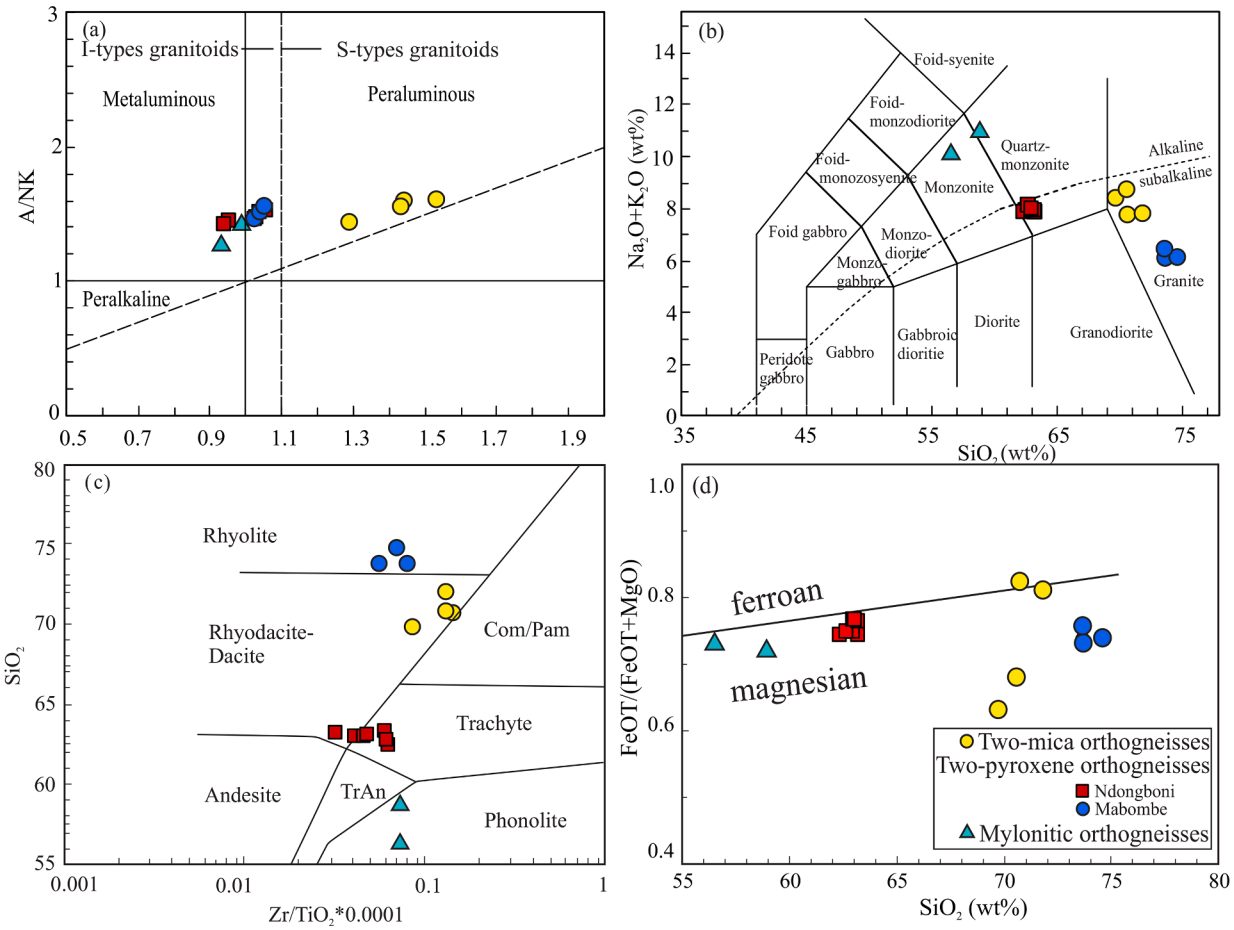

Fig. 6. Geochemical classifications of the two-mica, two-pyroxene and mylonitic orthogneisses from Nkondjock: (a) A/NK = $AL_2O_3/(Na_2O + K_2O)$ versus A/CNK = $AL_2O_3/(CaO + Na_2O + K_2O)$ (mole ratio) plot after (Maniar and Piccoli, 1989). Dashed line represents boundary between I- and S-type granites (Chappell and White, 1992). (b) $Na_2O + K_2O$ vs SiO_2 diagram after (Middlemost, 1994) (c)Immobile elements ($Zr/TiO_2 \times 0.0001$ versus SiO_2) rock classification diagram after (Winchester and Floyd, 1976).

5.3. Isotope geochemistry

Five samples were analyzed for whole rock Sr-Nd isotopic analyses and the results are presented in Table 4. Initial Sr-Nd isotopic compositions ratios were calculated back to their crystallization age. Two-mica orthogneiss have high initial $^{87}Sr/^{86}Sr$ ratios (0.70684, exception of the unrealistically low 0.68362 due to alteration effect), their measured and initial $^{143}Nd/^{144}Nd$ ratios range from 0.511806 to 0.511962 and from 0.511390 to 0.511497, respectively and their negative εNd(t) ranging from −8.6 to −6.5. Their two-stage model ages (T_{DM2}) for Nd isotope vary from 1862 to 2031 Ma (Table 4). Two-pyroxene orthogneiss have constant initial $^{87}Sr/^{86}Sr$ (0.71017–0.71063) ratios. Their measured and initial $^{143}Nd/^{144}Nd$ ratios range from 0.511636 to 0.511656 and from 0.511230 to 0.511293, respectively. They have negative εNd(t) (−12.1 to − 10.9) values and yield two-stage Paleoproterozoic Nd model ages of 2204–2304 Ma (Table 4). Mylonitic orthogneisses show similar Sr-Nd isotopic composition for the studied two-pyroxene orthogneiss. The analyzed mylonitic orthogneiss has high initial $^{87}Sr/^{86}Sr$ (0.70995) ratio and negative εNd(t) (−10.9), and the corresponding two-stage Nd model age is 2220 Ma (Table 4).

6. Discussion

6.1. Alteration effects

The studied samples have slightly high yet variable Loss on Ignition (LOI, 0.48–2.96%) probably due to different degrees of alteration, or metamorphism as can be inferred from a handful of chloritization, sericitization and uralitization observed in thin sections (Fig. 4i). Zirconium (Zr), widely considered as an immobile element, is often used to evaluate the mobility of geochemical element during post-magmatism overprint (Pearce and Peate, 1995; Wang et al., 2018). Considering that some large ion lithophile elements (e.g. Rb and Sr) do not show well-defined linear correlation with Zr (Fig. 11a and b), it is likely that such elements were mobilized during metamorphism. In contrast, HFSE (Y, Nb), REE (Nd, La), Th and transition elements (FeOt, TiO_2) show linear correlation with Zr (Fig. 11) and hence may have remained their primitive concentrations. In addition, most samples have constant chondritic normalized REE and the primitive mantle normalized multi-elements patterns (Fig. 7), further substantiating their being relatively immobile. Therefore, only immobile elements (REE, HFSE and some transitional elements) will be used to discuss the petrogenesis and geodynamic implication of the studied orthogneisses.

6.2. Timing of magma emplacement in the Nkondjock area

Three age groups are identified for the studied rocks of the Nkondjock area: (1) Neoproterozoic ages that are characteristic of two-mica, two-pyroxenes orthogneisses protoliths and mylonitic orthogneisses (2) Early Neoproterozoic magmatic zircon ages and Paleoproterozoic inherited zircon ages in mylonitic orthogneisses protolith. The Neoproterozoic ages of the two-mica (kk-1), two-pyroxene (kk-4) and the mylonitic orthogneisses (kk-14) protoliths (607 ± 4.8 Ma, 624.4 ± 3.5 Ma, 621 ± 9.1 Ma) can respectively be considered as ages of

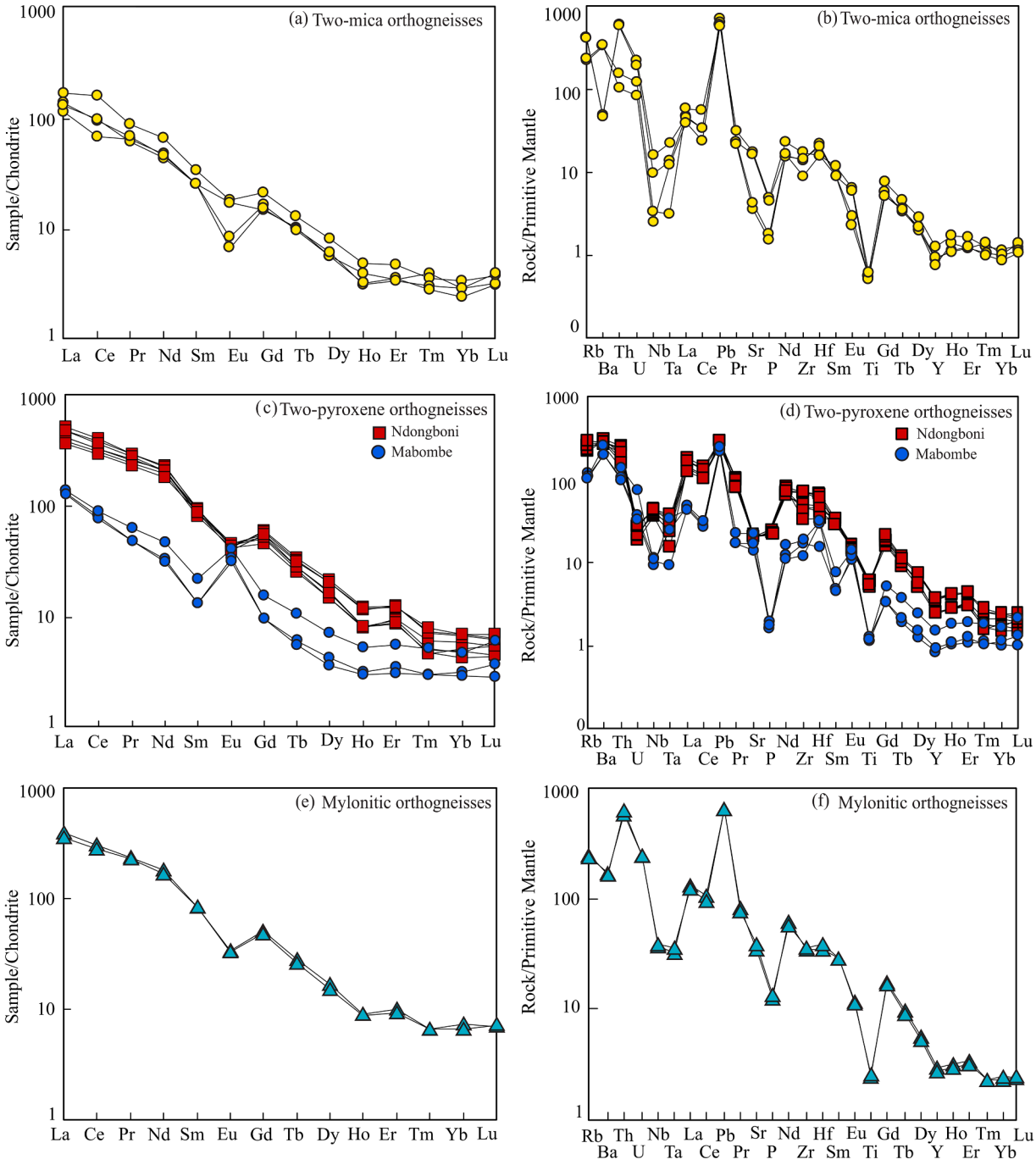

Fig. 7. Chondrite normalized REE plots (a, c, e) and primitive-mantle-normalized multi-element (b, d, f) patterns for two-mica, two-pyroxene, mylonitic orthogneisses samples. Normalizing values from Sun and McDonough (1989).

crystallization of magmatic protoliths of these orthogneisses as revealed by their high Th/U ratios (>0.1) and preserved igneous internal structures (Fig. 5). Inherited Paleoproterozoic zircon grains (2035–2099 Ma) of mylonitic orthogneisses indicate that their source rocks were emplaced during the Eburnean orogeny and reworked during the Pan-African orogeny. It has been considered that Eburnean inheritance is a common feature for intrusive rocks of West Cameroon (Li et al., 2017).

6.3. Nature of protoliths of the Nkondjock gneisses

Two-mica and two-pyroxene gneiss are considered as granitoids according to geochemical compositions (Fig. 6b). In general, granitoids are generally subdivided into I-, S-, M- and A-type depending on their chemical features and mineral modes (Chappell, 1999; Chappell and White, 1974). Two-mica orthogneisses samples fall within the magnesian field of the $FeO^t/(FeO^t + MgO)$ vs. SiO_2 diagram (Fig. 6d), suggesting that they do not belong to A-type granitoid, which is further substantiated with their low 10000 Ga/Al ratios (2.02–2.26). Also, they exhibit low εNd(t) (−8.6 and − 6.5) and high initial $^{87}Sr/^{86}Sr$ (0.70684) also suggesting S-type (Chappell and White, 1974) rather than M-type affinity (Whattam et al., 2016). Two-mica orthogneisses have high A/CNK (1.29–1.53) values (Fig. 6a) and high amount of biotite, alumina-minerals, such as muscovite in thin sections, suggesting that they were originally S-type granitoids (Chappell, 1999; Chappell and White, 1974). Geochemically, the protolith of two-pyroxene orthogneiss can be classified as I-type granitoids, as evidence they exhibit metaluminous to

Table 4
Whole Rock Sr-Nd isotope Compositions of Nkondjock gneisses.

Sample	lithology	Age (Ma)	Rb (ppm)	Sr (ppm)	$^{87}Rb/^{86}Sr$	$^{87}Sr/^{86}Sr$	±2σ	$^{87}Sr/^{86}Sr_i$	Sm ppm)	Nd (ppm)	$^{147}Sm/^{144}Nd$	$^{143}Nd/^{144}Nd$	±2σ	εNd(t)	T^{s}_{DM2} (Ga)
KK1-01	Two-mica gneiss	624	139	376	1.07	0.716374	0.000016	0.70684	5.27	31.3	0.101739	0.511806	0.000018	−8.6	2031
KK2-02		624	275	77	10.4	0.776250	0.000014	0.68362	3.95	21.0	0.113657	0.511962	0.000023	−6.5	1862
KK4-01	Two-pyroxene gneiss	607	164	421	1.13	0.719947	0.000011	0.71017	13.2	96.5	0.082655	0.511656	0.000011	−12.1	2304
KK5-02		607	160	432	1.07	0.719918	0.000013	0.71063	14.1	98.8	0.086112	0.511636	0.000021	−10.9	2204
KK14-01	Mylonitic gneiss	621	144	741	0.56	0.714938	0.000013	0.70995	12.8	84.5	0.091532	0.511645	0.000008	−10.9	2220

Note: $T_{DM2} = Ln((^{143}Nd/^{144}Nd\text{-}^{143}Nd/^{144}Nd_{DM}\text{-}(^{147}Sm/^{144}Nd_{Crust})*(EXP(\lambda^{147}Sm*rocks\ ages*10^6)\text{-}1))/(^{147}Sm/^{144}Nd_{Crust}\text{-}^{147}Sm/^{144}Nd_{DM}) + 1)/(\lambda^{147}Sm*10^6)$.
$^{143}Nd/^{144}Nd_{CHUR} = ^{143}Nd/^{144}Nd_{CHUR}\text{-}^{147}Sm/^{144}Nd_{CHUR}*(EXP(\lambda^{147}Sm*Rock\ age*1000000)\text{-}1)$.
$^{143}Nd/^{144}Nd_{CHUR} = 0.512630 \pm 11$ and $^{147}Sm/^{144}Nd_{CHUR} = 0.1960 \pm 4$ (Bouvier et al., 2008).

weakly peraluminous with A/CNK value of 0.88 to 1.06 (Fig. 6a) with relatively low SiO_2 content <70 wt% and decrease of P_2O_5 along with increasing SiO_2 (Fig. 10f), as well as positive correlation between yttrium, thorium and rubidium (Fig. 10g, h). Additionally, the presence of original pyroxene crystal further suggests that these granitoids have I-type affinity (Fig. 4f, g). In addition, the decreasing of A/CNK of two-pyroxene orthogneisses with increasing Mg + Fe (mol) strengthen that they have I-type granite characteristic (Fig. 8b, (Clemens and Stevens, 2012). In the A-B [(A = Al-(K + Na + 2Ca), B = Fe + Mg + Ti)] granite classification diagram (Fig. 8a) (Villaseca et al., 1998), the two-mica and two-pyroxene orthogneisses also plot in the S-type and I-type granites field, respectively, although some major oxides may be altered to some extent during the post-magmatism overprint processes.

Alternatively, mylonitic orthogneisses are considered as monzonite to quartz monzonite belonging to alkaline-series rocks (Fig. 6b), which is consistent with the trace element geochemical characteristic (high Zr/TiO_2 ratio, Fig. 6c). These mylonitic orthogneisses could also be lithologically composite due to different tectonics event that affected the rock and hence, can adequately explain the heterogeneous zircon Hf isotopic ratios in this rock.

6.4. Petrogenesis of the protolith of the Nkondjock orthogneisses

6.4.1. Petrogenesis of S-type two-mica orthogneisses

S-type granitoids are generally considered as deriving from (meta) sedimentary or supracrustal source. However, they show positive zircon εHf(t) varying from +2.9 to +5.2, which is decoupled from whole rock Nd isotopic compositions. This decoupling of Hf-Nd isotopic signatures can be explained by several mechanisms: 1) melt-peridotite interaction in the magma source of mantle-derived rocks (Bizimis et al., 2004), (2) coexistence of garnet during zircon crystallization from magma (Vervoort et al., 2000), 3) seawater involvement prior to partial melting of source rocks (van de Flierdt et al., 2002). Melt-peridotite interaction is not necessary to generate S-type magma and hence can be ruled out as one of the plausible mechanisms attached to Hf-Nd decoupling in this study. As suggested by (Vervoort et al., 2000), residual or cumulate garnet found in the lower crust could trigger decoupling of Hf-Nd isotope. Depletion of HREE relative to LREE observed for the two-mica orthogneisses in Nkondjock region (Fig. 7a) can either imply the presence of residual garnet in their source or geochemical differentiation during partial melting (Wu et al., 2006), which is further constrained by elevated La/Yb_N and Sr/Y ratios of two-mica orthogneisses (Rapp et al., 1991).

6.4.2. Petrogenesis of I-type two-pyroxene orthogneisses

Several petrogenesis models have being suggested for the origin of I-type granitoids, such as (a) partial melting of mixed crust-mantle materials in the lower crust and subsequent fractional crystallization of the melts (Chappell et al., 2012), (b) a complete fractional crystallization of mantle derived magma (Li et al., 2007) and (c) partial melting of the metaigneous protolith (Chappell and White, 2001; Huang et al., 2018).

Two-pyroxene and mylonitic orthogneisses have negative whole rock εNd(t) values (−12.1 to − 10.9) and zircon εHf(t) (−19.2 to − 1), precluding the possibility of a complete fractional crystallization of mantle derived melts for these protoliths. Most of the grains have very negative εHf(t) (−19.2 to −10.7) and $^{176}Hf/^{177}Hf$ varying (0.281162 to 0.282322). This interpretation is also reinforced with εNd(t) vs $^{87}Sr/^{86}Sr_i$ diagram where these samples plots in the lower continental crust area, implying partial melting of old continental crust (Fig. 13a). We thus conclude that a mature continental crust is likely the source of two-pyroxenes and mylonitic orthogneisses.

High P-T experimental studies display that melts derived from low-K metabasalts in the lower crust are usually intermediate to felsic in composition with low K_2O contents and K_2O/Na_2O ratios (<1) (Rapp and Watson, 1995). The protolith of Nkondjock orthogneisses have low MgO (0.21–0.50 wt%) values, variable K_2O (1.96–5.98 wt%) and high

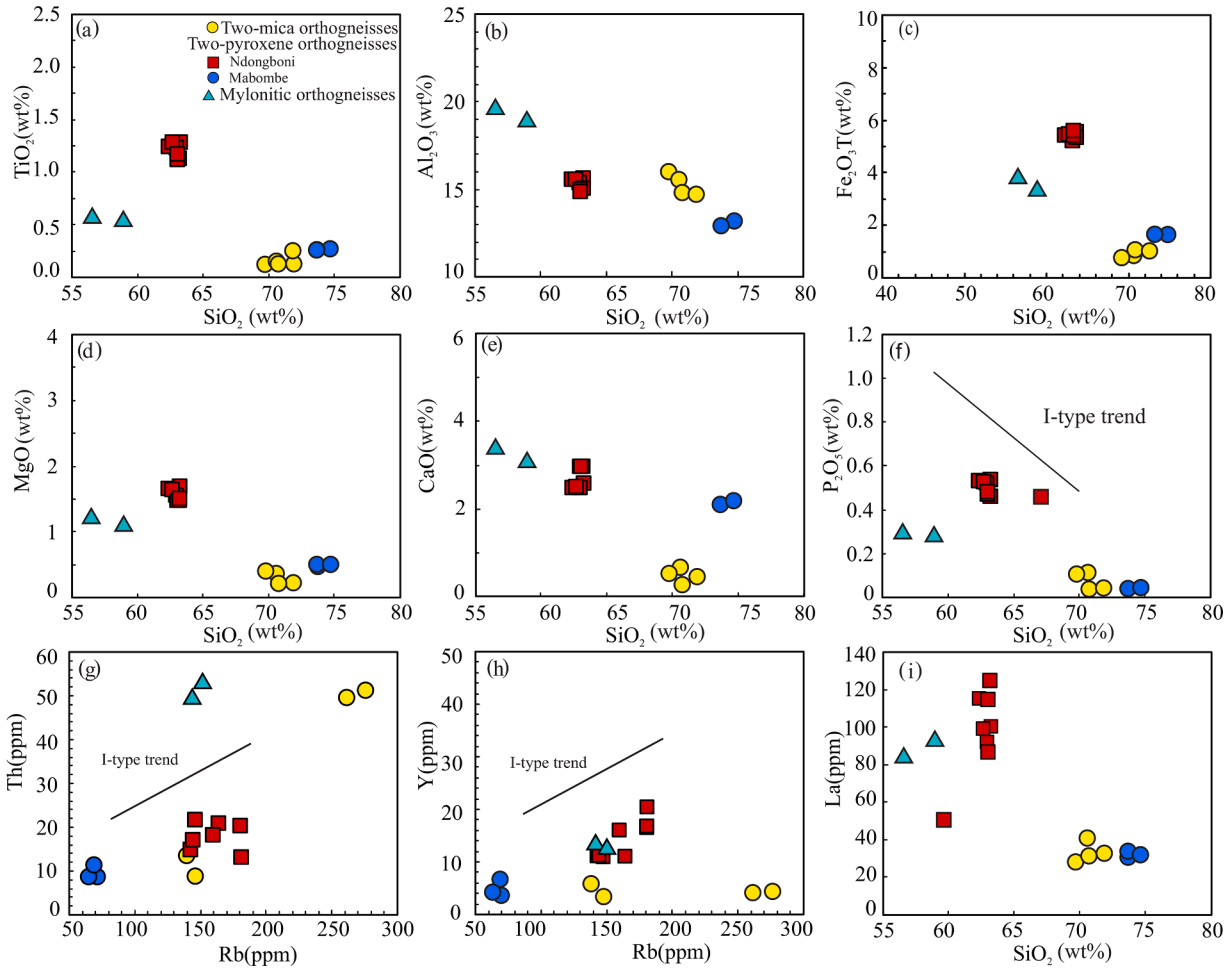

Fig. 8. (a) A-B granite classification diagram for the studied granites, modified from (Villaseca et al., 1998). The parameters are expressed as gram-atoms × 103 of each element in 100 g of material. The blue dotted line represents the boundary between I- and S-type granites. (b) diagram showing covariance between A/CNK value and maficity index (Fe + Mg; moles of per 100 g rock material) and S-type granites characteristic. (For interpretation of the references to color in this figure legend, the reader is referred to the web version of this article.)

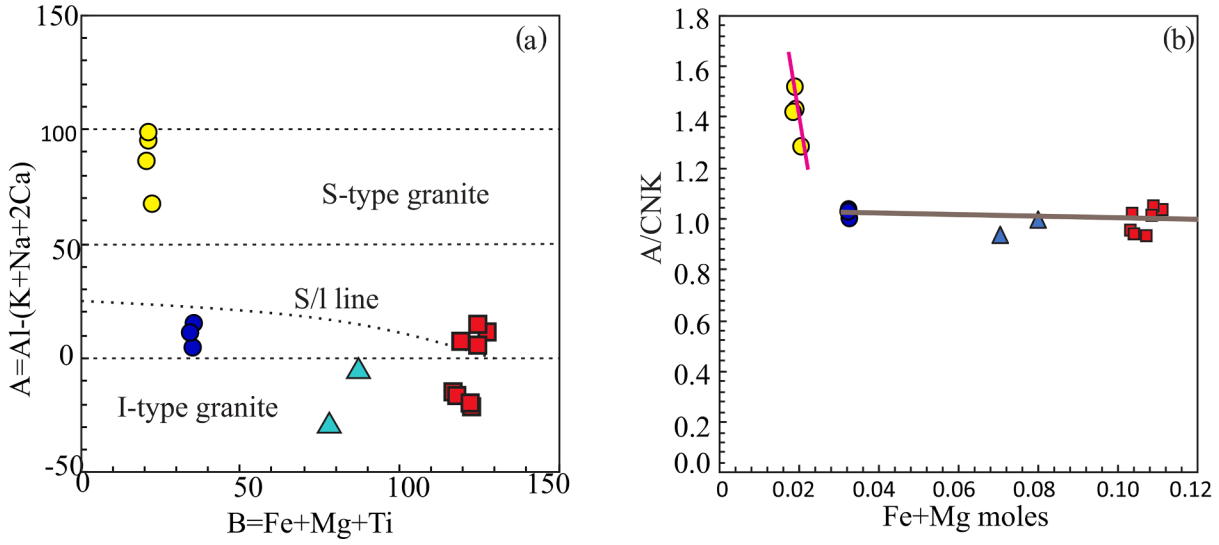

Fig. 9. Yb versus Ta diagram after (Pearce et al., 1984) tectonic discrimination diagram for two-mica, two-pyroxene and Mylonitic orthogneisses.

Na_2O (3.10–5.01 wt%) contents, similar to above experimental melts. Geochemical characteristics of Pan-African granitoids in Western Cameroon indicate that the lower crust metabasites in western Cameroon are dominated by high-K calc-alcalic to shoshonitic series (Djouka-Fonkwé et al., 2008). Hence, we suggest that the two-pyroxene orthogneiss from Nkondjock was formed by partial melting of thickened

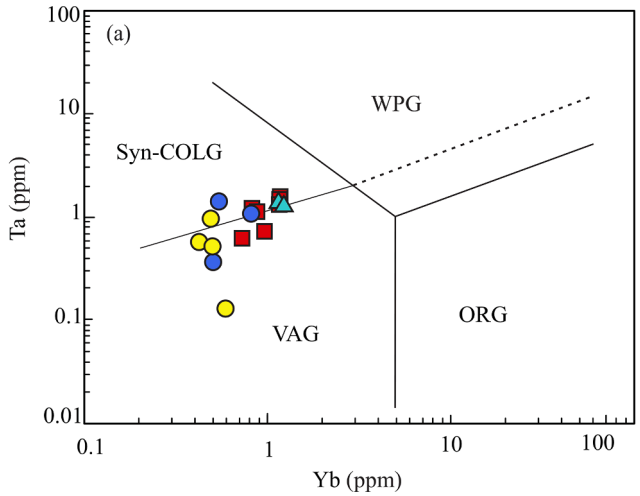

Fig. 10. Harker variation diagram showing major and trace element with SiO_2 variation of two-mica, two-pyroxene and mylonitic orthogneisses from Nkondjock area.

lower crust with subsequent crystal fractionalization.

6.5. Implication of the Pan-African crustal thickening

The studied orthogneisses show some adakitic affinities, such as depletion on heavy rare earth elements (HREEs) (e.g. Yb = 0.42–0.81, $(La/Yb)_N$ = 29.7 to 55.6), low Mg# (30.8 to 55). These samples also fall within the adakitic field on discrimination diagram of $(La/Yb)_N$ versus Yb_N (Fig. 12b) according to (Defant and Drummond, 1990). Subduction of hot oceanic plates was previously considered as the only origin of adakites, however, some researchers recently have proposed different tectonic settings and models for their origin, such as assimilation and fractional crystallization (AFC) processes involving basaltic magma, partial melting of thickened lower crust, delaminated mafic lower crust and slab window process (Zhang et al., 2010).

The strong depletion in HREE and Y compositional characteristics generally fit with slab-derived magmas (Atherton and Petford, 1993), however, the studied orthogneisses with adakitic signature are peraluminous and have variable Mg# value (30.8 to 55) and Ni contents (3.73 to 48.7 ppm), contrasting to oceanic slab-derived adakite melts which is generally metaluminous (Smithies and Champion, 2000). Their low εNd(t) range from −6.5 to −10.9 and high $^{87}Sr/^{86}Sr_i$ ratios range from 0.70684 to 0.71063 (Table 4), further implying precipitation of mature crustal source. In addition, the age of these two-mica and two-pyroxene orthogneisses (624.4 ± 3.5 Ma and 607 ± 4.8 Ma) correlate within error with the timing suggested by both (Toteu et al., 2004) for a collision event between the northern part of the Congo craton and the West African craton during the Pan-African D_1 to D_3 events (640–580 Ma) and (Li et al., 2017) who dated the *syn*-collisional D2 event from 620 to 600 Ma. All these features preclude an oceanic curst scenario and the possibility of being produced by oceanic slab derived-melt.

Adakitic melts can also be produced by fractionation crystallization from a parental basaltic magma under a variety of pressure conditions (Castillo et al., 1999; Macpherson et al., 2006). Negative Eu and Sr anomalies and no concave-upward patterns on the MREE (middle rare earth elements) of two-mica orthogneisses (Fig. 7a) suggest fractional crystallization of plagioclase and/or amphibole, contrary to Mabombé two-pyroxene orthogneisses which show positive Eu and Sr anomalies and clear concave-upwards patterns (Fig. 7c). However, in the Al_2O_3 and La vs SiO_2 diagram, the Mabombé two-pyroxene do not increase or decrease with increasing SiO_2 contents (Fig. 8b, i). Two-mica and the Mabombé two-pyroxene orthogneisses from the Nkondjock area have low MgO (0.21–0.50 wt%) and moderate Mg# (30.8–55) suggesting that they did not derive directly from the mantle wedge (Atherton and Petford, 1993). Their low MgO content and Mg# are similar to the experimental melts of metabasalts and eclogites at 1.0–4.0 GPa (Rapp et al., 1999) and adakitic rocks produced by partial melting of the lower mafic crust worldwide (Fig. 12c). Indeed, they also show a trend similar to the metabasalt at 1.6 GPa of (Rapp and Watson, 1995) (Fig. 12d). Adopting these features, we propose partial melting of the lower crust as the most probable petrogenetic model for the protolith of these rocks (two-mica and the Mabombé two-pyroxene orthogneisses). This petrogenetic model is generally suggested to occur at >40 km (>1.2 GPa) (Atherton and Petford, 1993), meaning that the crustal thickness in the Nkondjock area was at least 40 km when the biotite and two-pyroxene gneisses adakitic magma was produced during the Pan-African. These data imply that the crust of the Nkondjock area was thicker (>40 km) during Neoproterozoic Pan-African era than the present crust (33 km) (Dorbath et al., 1984), therefore, the Nkondjock crust has most likely undergone a thinning process after Pan-African Orogenesis.

6.6. Geodynamic setting of late Neoproterozoic magmatism

Protoliths of the studied two-mica, two-pyroxene and mylonitic orthogneisses straddle between the *syn*-collision granites and the volcanic arc granites field (Fig. 9).

According to regional tectonic, the Pan-African D_2 deformation event resulting from the continental collision between the Congo Sao-Francisco cratons, the West African craton and the Saharan metacraton led to the formation of widespread orthogneisses in West Cameroon (Toteu et al., 2004). Toteu et al. (2004) dated the D_2 deformation between 640 and 610 Ma, which was further constrained by (Li et al., 2017) between 620 and 600 Ma. The Neoproterozoic ages of the biotite, two-pyroxene and the Mylonitic orthogneisses (624.4 ± 3.5,607 ± 4.8 Ma and 621 ± 9.1 Ma) correlate within error to the timing of regional D_2 deformation (Li et al., 2017; Toteu et al., 2004). Furthermore, bimodal distribution (crust-mantle) for the Nkondjock orthogneisses can be considered as the result of interaction between the lower crust and the mantle during the end of the slab break off. (Loose and Schenk, 2018) interpret eclogites and metabasites sampled at ca. 150 km to the SW of the studied area as former ocean floor basalts and that the corridor bearing such rocks likely marks a subduction zone formed at around 2.09 Ga during the Paleoproterozoic. Recent works in west Cameroon (Tchouankoue et al., 2016) and south east Nigeria (Ugwuonah et al., 2019) provided many evidence of the existence of a subduction environment within an NNE-SSW geodynamic environment. Isotopic results indicate Paleoproterozoic model ages of Nkondjock orthogneisses present a source distinct from Archean rocks from the Congo craton (2900–3000 Ma) represented in Cameroon by the Ntem complex situated in the Northern part of the Congo craton.

6.7. Implications for geodynamics at the northern border of the Congo craton in Cameroon

On the geology map of Cameroon (Fig. 1b), the SSW-NNE oriented Tcholliré -Banyo Fault (TBF) delineates elongated small to medium size Neoproterozoic granitoids in North (Nomo et al., 2017; Saha-Fouotsa et al., 2019), West Cameroon (Djouka-Fonkwé et al., 2008; Kwékam et al., 2015; Njiekak et al., 2008) and batholithic granitoids of the Adamawa-Yadé massif with inherited Archean ages (Ganwa et al., 2016; Tchakounté et al., 2017). Rocks of the Nkondjock region border to the SSW the corridor of the Banyo-Tcholliré and recent detailed works in the Bafia region at ca. 100 km to the SE of the studied area pointed out to the permanence of inherited Archean ages (Tchakounté et al., 2017). They concluded that the Bafia region was part of a single craton (Adamawa-Yadé) detached from the Congo craton and imprinted by later Eburnean (Paleoproterozoic) and Pan-African (Neoproterozoic) orogenies. Contrary to rocks of the Bafia area, studied rocks in the Nkondjock region show only Paleoproterozoic oldest ages (zircons U-Pb or Nd T_{DM} ages).

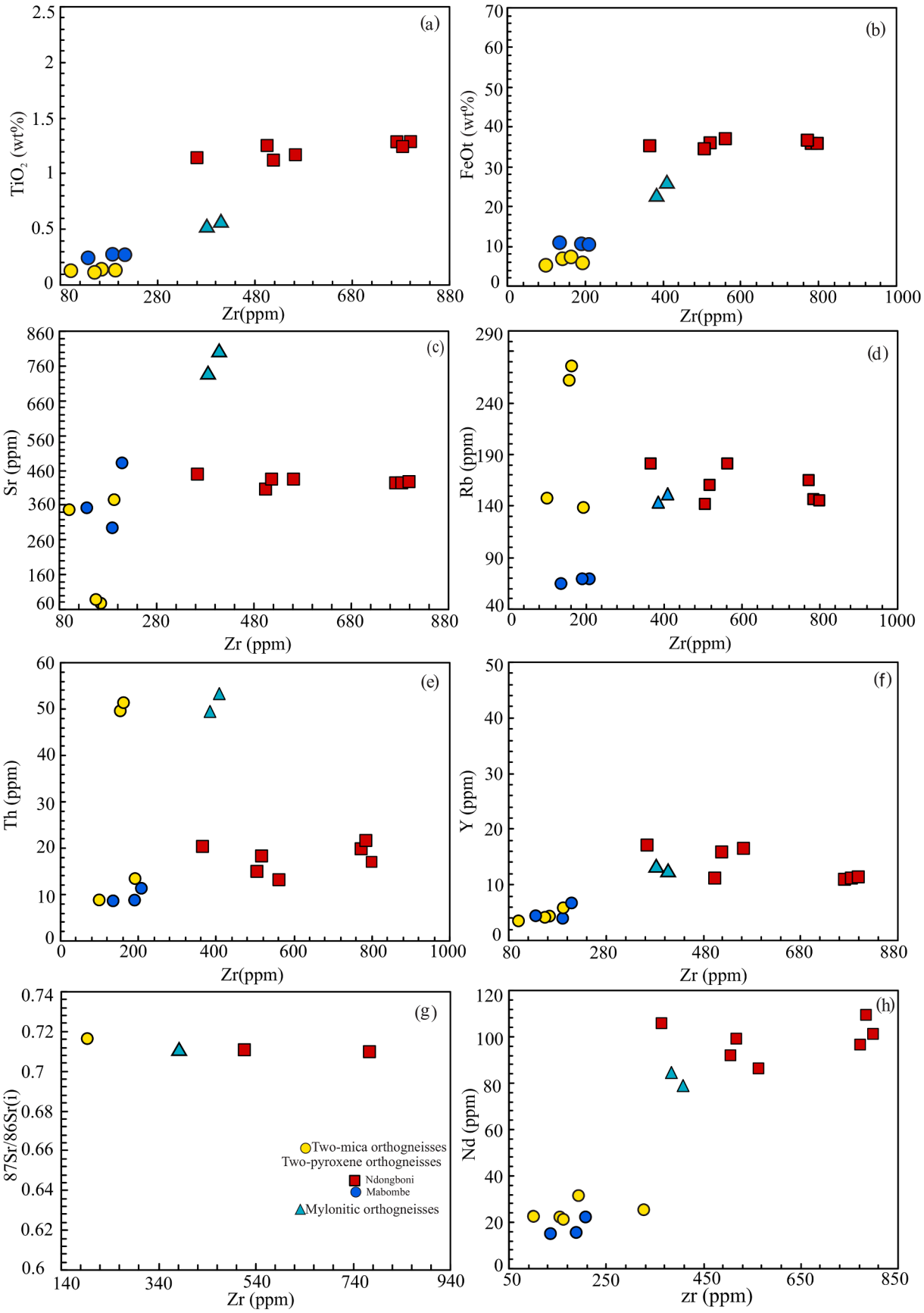

Fig. 11. Zr versus (TiO_2, FeO^t, Sr, Th, Y, Nd, $^{87}Sr/^{86}Sr_i$) to evaluate the mobility of these elements including (LILE, REE and HFSE) during alteration.

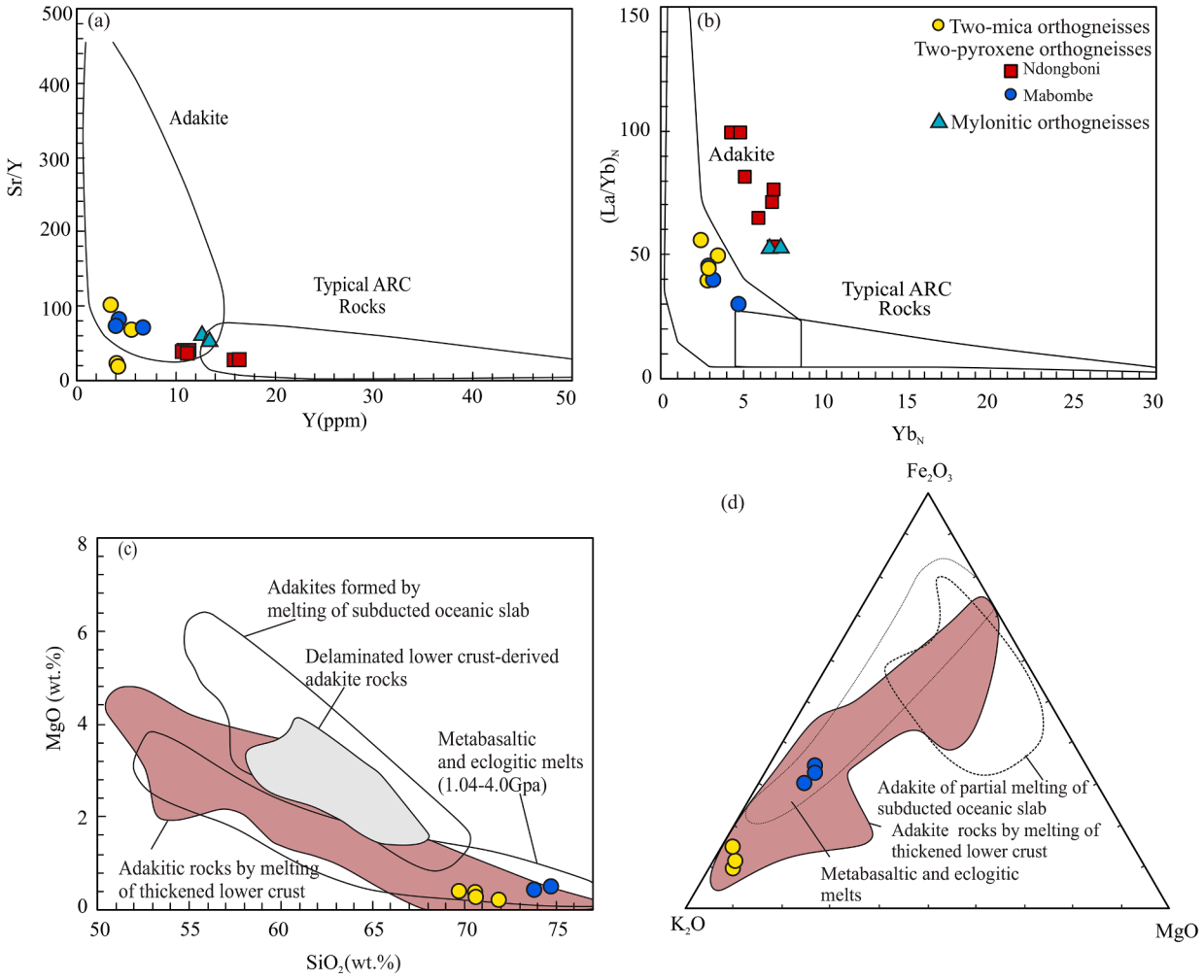

Fig. 12. Plots of Sr/Y vs Y (a) La/Yb_N vs Yb_N (b) discrimination diagram for the adakite from the Nkondjock area. Adakitic and non-arc field after (Defant and Drummond, 1990). (c) MgO vs SiO_2 diagram for the gneisses of the Nkondjock area. The adakites produced by melting of oceanic slabs, delamination of lower crust, and metabasaltic and experimental melts (1–4.0 Gpa) (Karsli et al., 2011). Adakites formed by melting of lower crust are the reference field (Karsli et al., 2011). (d) Ternary diagrams of Fe_2O_3-MgO-K_2O for the orthogneisses from Nkondjock region. The grey field represents experimental melts of metabasalts at 16–22 Gbar (Rapp and Watson, 1995).

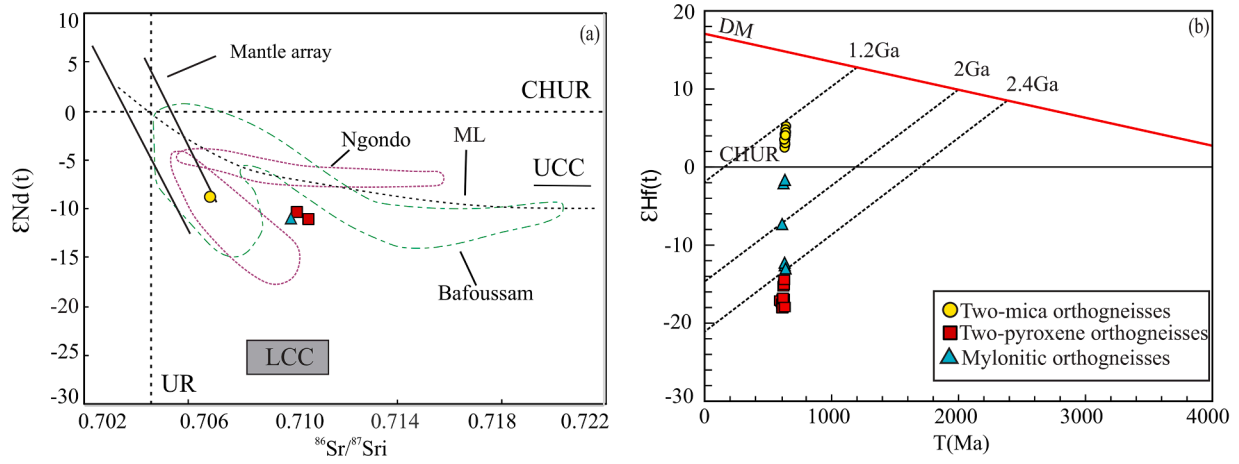

Fig. 13. (a) εNd (600 Ma) vs $^{86}Sr/^{87}Sr$ (600 Ma) LCC, Lower continental Crust; Ucc upper continental crust from (Liégeois et al., 2013) , Ndongo granites (Tagne-Kamga, 2003), Bafoussam granites (Djouka-Fonkwé et al., 2008), CHUR, chondrite uniform reservoir, UR, Uniform reservoir Ml mixing line between depleted mantle and continental crust sources recognized from Lachlan I- and S-type granitoids by (McCulloch and Chappell, 1982). (b) Plot of εHf (t) vs age for zircons from the gneisses from Nkondjock area. CHUR = chondritic uniform reservoir; DM = depleted mantle. The corresponding lines of crustal extraction are calculated by using the $^{176}Lu/^{177}Hf$ ratio of 0.015 for the average continental crust (Griffin et al., 2000).

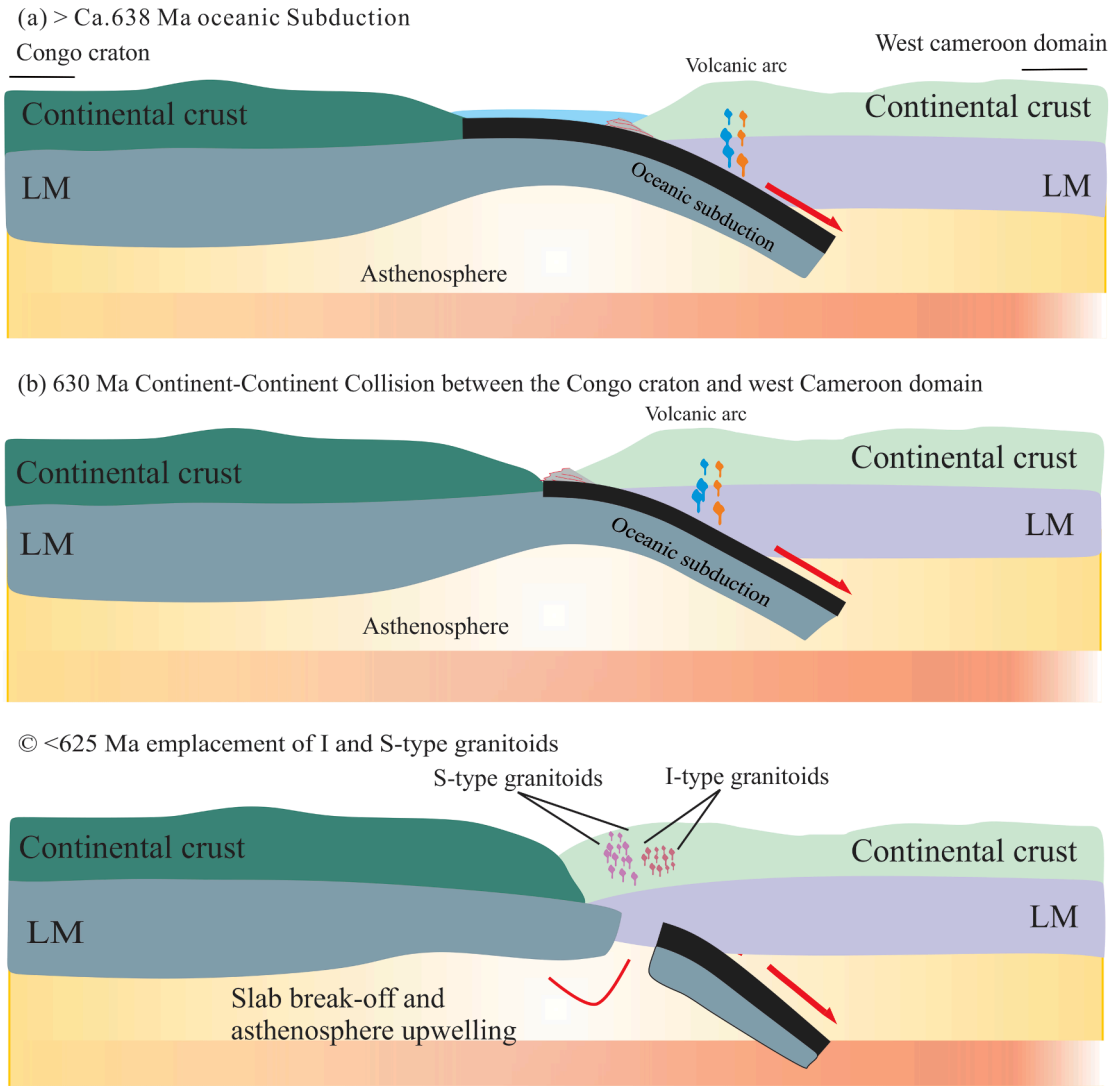

Fig. 14. The proposed three-stage *syn*-collisional preceding subduction model for the geodynamic evolution of Nkondjock gneisses. (a) oceanic crust subduction ca. > 638 Ma (b) beginning of the collision and initiation of slab-break off (c) partial melting of thickened lower crust due to the upwelling of the asthenosphere and emplacement of S and I-type granitoids. Congo Craton (CC); West Cameroon Domain (WCD); Lower Crust (LC); Lithospheric Mantle (LM).

We can thus conclude that the studied rocks formed during the convergence between the Congo craton and the west African craton and that the Congo craton did not contribute to the generation of the Neoproterozoic crust.

We propose a three stage-model to explain the petrogenesis of I- and S-type granitoids, throughout a possible northwesternward subduction-collision system that led to the emplacement of I- and S-type granitoids during crustal melting and collision of orthogneissic rocks in the Nkondjock area (Fig. 14). Subduction of the oceanic slab beneath the continental margin of the West Cameroon domain occurred at ca. > 638 Ma (Fig. 14a). Detachment of the oceanic slab, continental collision and slab break-off induced the upwelling of the asthenosphere which heated the thickened lower crust and initiated partial melting, at ca. 625 Ma with contribution of the lithospheric mantle (Fig. 14b). I- and S-type granites were emplaced during the collision of the two blocks < 625 Ma in the Nkondjock region (Fig. 14c).

The potential magma source for S- and I-type granitoids is partial melting of thickened lower crust at NdT_{DM2} = 1.9–2 Ga. These results are consistent with the Sm-Nd isotopic data reported by (Toteu et al., 2001) from Pan-African granitoids from Southeast of the TBF which they suggested to have been generated by melting of older crust (Eburnean) with limited juvenile input. (Djouka-Fonkwé et al., 2008; Tagne-Kamga, 2003) also reported for the Ngondo and the Bafoussam complex situated respectively at 150 km and 100 km to the NE and NNE of the studied area a partial melting of heterogeneous (meta)-igneous mafic lower crustal materials for their source (Fig. 14a). (Chung et al., 2003; Karsli et al., 2011) suggested that when adakites are formed by the partial melting of a mafic lower continental crust they can either be eclogites or garnet amphibole. Biotite orthogneisses shows no concave upwards on their HREE patterns which suggest that amphibole played a more important role than garnet during partial melting (Rollinson, 1993). Furthermore, the HREE of two-pyroxene (Mabombé) orthogneisses shows concave upwards patterns. In summary we suggest that garnet-amphibole is likely to be the source of lithology and that these orthogneisses were formed by partial melting of a thickened, garnet bearing, amphibolitic lower continental crust with some lithospheric mantle input.

7. Conclusions:

1) Petrographically, three main rock facies that constitute the basement of Pan-African granitoids of West Cameroon were identified in the studied area: dominant two-mica orthogneisses and minor two-pyroxene and mylonitic orthogneisses. Geochronology result shows

that these rocks are formed at 607 ± 4.8–624.4 ± 3.5 Ma, which correlate with the Pan-African orogeny which affected the whole West Cameroon between 630 and 583 Ma.
2) Whole-rock geochemistry and the Sr-Nd-Hf isotopic data indicate S-type two-mica and I-type two-pyroxene (Mabombé) orthogneisses were generated by partial melting of the garnet-bearing heterogeneous lower continental crust with minor mantle input.
3) The studied S- and I-type granitoids were emplaced during the collision between the Congo and the west African craton (638–624 Ma) through partial melting garnet-bearing heterogeneous lower continental crust in response to the upwelling of asthenosphere, possibly triggered by the slab break off (<638 Ma).

CRediT authorship contribution statement

M.S Kamguia Kamani: Conceptualization, Investigation, Writing - original draft. **Wei Wang:** Conceptualization, Investigation, Supervision, Writing - original draft. **J.-P Tchouankoue:** Writing - review & editing. **Si-Fang Huang:** Investigation, Data curation, Writing - review & editing. **B Yomeun:** Investigation, Data curation, Writing - review & editing. **Er-Kun Xue:** Investigation, Data curation, Writing - review & editing. **Gui-Mei Lu:** Investigation, Data curation, Writing - review & editing.

Declaration of Competing Interest

The authors declare that they have no known competing financial interests or personal relationships that could have appeared to influence the work reported in this paper.

Acknowledgments

This study was supported by National Natural Science Foundation of China (NSFC 41972242) the MOST Special Fund from the State Key Laboratory of Geological Processes and Mineral Resources (MSFGPMR 01-1) and the Fundamental Research Funds for the Central Universities (CUGCJ1709), China University of Geosciences (Wuhan). We thank Zhaochu Hu for the (MC)-LA-ICPMS analyses and Abing Lin for the whole-rock geochemical analyses. Constructive comments from two anonymous reviews and associated editor Dr. Kamal Ali are important and helpful in improving the manuscript.

Appendix A. Supplementary data

Supplementary data to this article can be found online at https://doi.org/10.1016/j.precamres.2020.106015.

References

Abdelsalam, M.G., Liégeois, J.-P., Stern, R.J., 2002. The Saharan Metacraton. J. Afr. Earth Sc. 34, 119–136.
Atherton, M.P., Petford, N., 1993. Generation of sodium-rich magmas from newly underplated basaltic crust. Nature 362, 144–146.
Bizimis, M., Sen, G., Salters, V.J.M., 2004. Hf–Nd isotope decoupling in the oceanic lithosphere: constraints from spinel peridotites from Oahu, Hawaii. Earth Planet. Sci. Lett. 217, 43–58.
Blichert-Toft, J., Albarède, F., 1997. The Lu-Hf isotope geochemistry of chondrites and the evolution of the mantle-crust system. Earth Planet. Sci. Lett. 148, 243–258.
Bouvier, A., Vervoort, J.D., Patchett, P.J., 2008. The Lu–Hf and Sm–Nd isotopic composition of CHUR: Constraints from unequilibrated chondrites and implications for the bulk composition of terrestrial planets. Earth Planet. Sci. Lett. 273, 48–57.
Castaing, C., Feybesse, J.L., Thiéblemont, D., Triboulet, C., Chèvremont, P., 1994. Palaeogeographical reconstructions of the Pan-African/Brasiliano orogen: closure of an oceanic domain or intracontinental convergence between major blocks? Precambr. Res. 69, 327–344.
Castillo, P.R., Janney, P.E., Solidum, R.U., 1999. Petrology and geochemistry of Camiguin Island, southern Philippines: insights to the source of adakites and other lavas in a complex arc setting. Contrib. Miner. Petrol. 134, 33–51.
Chappell, B.W., 1999. Aluminium saturation in I- and S-type granites and the characterization of fractionated haplogranites. Lithos 46, 535–551.
Chappell, B.W., White, A.J.R., 1974. Two contrasting granite types. Pacif. Geol. 8, 173–174.
Chappell, B.W., Bryant, C.J., Wyborn, D., 2012. Peraluminous I-type granites. Lithos 153, 142–153.
Chappell, B.W., White, A.J.R., 1992. I- and S-type granites in the Lachlan Fold Belt. Earth Environ. Sci. Trans. Royal Soc. Edinburgh 83, 1–26.
Chappell, B.W., White, A.J.R., 2001. Two contrasting granite types: 25 years later. Aust. J. Earth Sci. 48, 489–499.
Chen, F., Li, X.-H., Wang, X.-L., Li, Q.-L., Siebel, W., 2007. Zircon age and Nd–Hf isotopic composition of the Yunnan Tethyan belt, southwestern China. Int. J. Earth Sci. 96, 1179–1194.
Chen, F., Zhu, X., Wang, W., Wang, F., Hieu, P., Siebel, W., 2009. Single-grain detrital muscovite Rb-Sr isotopic composition as an indicator of provenance for the Carboniferous sedimentary rocks in northern Dabie, China. Geochem. J. 43 (4), 257–273.
Chung, S.-L., Liu, D., Ji, J., Chu, M.-F., Lee, H.-Y., Wen, D.-J., Lo, C.-H., Lee, T.-Y., Qian, Q., Zhang, Q., 2003. Adakites from continental collision zones: Melting of thickened lower crust beneath southern Tibet. Geology 31, 1021–1024.
Clemens, J.D., Stevens, G., 2012. What controls chemical variation in granitic magmas? Lithos 134–135, 317–329.
Defant, M.J., Drummond, M.S., 1990. Derivation of some modern arc magmas by melting of young subducted lithosphere. Nature 347, 662–665.
Djouka-Fonkwé, M.L., Schulz, B., Schüssler, U., Tchouankoué, J.P., Nzolang, C., 2008. Geochemistry of the Bafoussam Pan-African I- and S-type granitoids in western Cameroon. J. Afr. Earth Sc. 50, 148–167.
Dorbath, L., Dorbath, C., Stuart, G., Fairhead, D., 1984. Structure de la croute sous le plateau de l'adamaoua (Cameroun). C.R. Acad. Sci. Paris 298, 539–542.
Dumort, J.C., 1968. Carte géologique de reconnaissance du Cameroun à l'échelle 1/500000, coupure Douala-Ouest avec une notice explicative. Bull. direction de géologie et des mines, Cameroun, p. 60p.
Fitzsimons, I.C.W., 2003. Proterozoic basement provinces of southern and southwestern Australia, and their correlation with Antarctica. Geol. Soc. Lond. Spec. Publ. 206, 93.
Ganwa, A.A., Klötzli, U.S., Hauzenberger, C., 2016. Evidence for Archean inheritance in the pre-Panafrican crust of Central Cameroon: Insight from zircon internal structure and LA-MC-ICP-MS UPb ages. J. Afr. Earth Sc. 120, 12–22.
Griffin, W. L., Pearson, N. J., Belousova, E., Jackson, S. E., Van Achterbergh, E., O'Reilly, S. Y., and Shee, S. R., 2000, The Hf isotope composition of cratonic mantle: LAM-MC-ICPMS analysis of zircon megacrysts in kimberlites: Geochim. Cosmochim. Acta 64 (1), 133–148.
Houketchang Bouyo, M., Penaye, J., Mouri, H., Toteu, S.F., 2019. Eclogite facies metabasites from the Paleoproterozoic Nyong Group, SW Cameroon: Mineralogical evidence and implications for a high-pressure metamorphism related to a subduction zone at the NW margin of the Archean Congo craton. J. Afr. Earth Sci. 149, 215–234.
Huang, S.F., Wang, W., Zhao, J.H., Zheng, J.P., 2018. Petrogenesis and geodynamic significance of the ~850 Ma Dongling A-type granites in South China. Lithos 318-319, 176–193. https://doi.org/10.1016/j.lithos.2018.08.016.
Jackson, S., Pearson, N., Griffin, W., Belousova, E., 2004. The application of laser ablation-inductively coupled plasma-mass spectrometry to in situ U-Pb zircon geochronology. Chem. Geol. 211, 47–69.
Kamga, G.T., Mercier, E., Rossy, M., N'Sifa, E.N., 1999. Synkinematic emplacement of the Pan-African Ngondo igneous complex (west Cameroon, central Africa). J. Afr. Earth Sc. 28, 675–691.
Karsli, O., Ketenci, M., Uysal, İ., Dokuz, A., Aydin, F., Chen, B., Kandemir, R., Wijbrans, J., 2011. Adakite-like granitoid porphyries in the Eastern Pontides, NE Turkey: Potential parental melts and geodynamic implications. Lithos 127, 354–372.
Kinny, P.D., Maas, R., 2003. Lu–Hf and Sm–Nd isotope systems in zircon. Rev. Mineral. Geochem. 53, 327–341.
Kusky, T.M., Abdelsalam, M., Tucker, R.D., Stern, R.J., 2003. Evolution of the East African and related orogens, and the assembly of Gondwana. Precambr. Res. 123, 81–85.
Kwékam, M., Affaton, P., Bruguier, O., Liégeois, J.-P., Hartmann, G., Njonfang, E., 2013. The Pan-African Kekem gabbro-norite (West-Cameroon), U-Pb zircon age, geochemistry and Sr–Nd isotopes: Geodynamical implication for the evolution of the Central African fold belt. J. Afr. Earth Sc. 84, 70–88.
Kwékam, M., Dunkl, I., Fozing, E.M., Hartmann, G., Njanko, T., Tcheumenak, K.J., Njonfang, E., 2020. Syn-kinematic ferroan high-K I-type granites from Dschang in southwestern Cameroon: U–Pb age, geochemistry and implications for crustal growth in the late Pan-African orogeny. Geological Society, London, Special Publications 502, SP502-2019-2019.
Kwékam, M., Hartmann, G., Njanko, T., Tcheumenak Kouémo, J., Fozing, E.M., Njonfang, E., 2015. Geochemistry and isotope Sr-Nd character of Dschang biotite granite implications for the Pan-African continental crust evolution in West-Cameroon (Central Africa). J. Earth Sci. Res. Can. 1, 88–102.
Kwékam, M., Liégeois, J.-P., Njonfang, E., Affaton, P., Hartmann, G., Tchoua, F., 2010. Nature, origin and significance of the Fomopéa Pan-African high-K calc-alkaline plutonic complex in the Central African fold belt (Cameroon). J. Afr. Earth Sci. 57, 79–95.
Lasserre, M., Soba, D., 1976. Ages cambriens des granites de Nyîbi et de Kongolo(Centre Est Cameroun). C. R. Acad. Sci. Paris 283, 1695–1698.
Li, X.-H., Chen, Y., Tchouankoue, J.P., Liu, C.-Z., Li, J., Ling, X.-X., Tang, G.-Q., Liu, Y., 2017. Improving geochronological framework of the Pan-African orogeny in Cameroon: New SIMS zircon and monazite U-Pb age constraints. Precambr. Res. 294, 307–321.
Li, X.-H., Li, Z.-X., Li, W.-X., Liu, Y., Yuan, C., Wei, G., Qi, C., 2007. U-Pb zircon, geochemical and Sr–Nd–Hf isotopic constraints on age and origin of Jurassic I- and

A-type granites from central Guangdong, SE China: A major igneous event in response to foundering of a subducted flat-slab? Lithos 96, 186–204.
Liégeois, J.-P., Abdelsalam, M.G., Ennih, N., Ouabadi, A., 2013. Metacraton: Nature, genesis and behavior. Gondwana Res. 23, 220–237.
Liu, Y.S., Gao, S., Hu, Z.C., Gao, C., Zong, K., Wang, D., 2010. Continental and oceanic crust recycling-induced melt-peridotite interactions in the Trans-North China Orogen: U-Pb Dating, Hf Isotopes and trace elements in zircons from mantle xenoliths. J. Petrol. 51 (1–2), 537–571.
Loose, D., Schenk, V., 2018. 2.09 Ga old eclogites in the Eburnian-Transamazonian orogen of southern Cameroon: Significance for Palaeoproterozoic plate tectonics. Precambr. Res. 304, 1–11.
Ludwig, K.R., 2003. Isoplot/Ex version 2.49: A Geochronological Toolkit for Microsoft Excel. Bekerly Geochronology Center Special. Publication 1–43.
Macpherson, C.G., Dreher, S.T., Thirlwall, M.F., 2006. Adakites without slab melting: High pressure differentiation of island arc magma, Mindanao, the Philippines. Earth Planet. Sci. Lett. 243, 581–593.
Maniar, P.D., Piccoli, P.M., 1989. Tectonic discrimination of granitoids. Geol. Soc. Am. Bull. 101, 635–643.
McCulloch, M.T., Chappell, B.W., 1982. Nd isotopic characteristics of S- and I-type granites. Earth Planet. Sci. Lett. 58, 51–64.
Middlemost, E.A.K., 1994. Naming materials in the magma/igneous rock system. Earth Sci. Rev. 37, 215–224.
Ngo Belnoun, R., Tchouankoue, J., Itiga, Z., Simeni Wambo, N.A., Owona, S., KollerThöni, M., 2013. Geochemistry of Bayon plutonic complex - Western Cameroon. Global J. Geol. Sci. 11, 73–93.
Njiekak, G., Dörr, W., Tchouankoué, J.-P., Zulauf, G., 2008. U-Pb zircon and microfabric data of (meta) granitoids of western Cameroon: Constraints on the timing of pluton emplacement and deformation in the Pan-African belt of central Africa. Lithos 102, 460–477.
Njonfang, E., Ngako, V., Kwekam, M., Affaton, P., 2006. Les orthogneiss calco-alcalins de Foumban-Bankim : témoins d'une zone interne de marge active panafricaine en cisaillement. C.R. Geosci. 338, 606–616.
Nkoumbou, C., Barbey, P., Yonta-Ngouné, C., Paquette, J.L., Villiéras, F., 2014. Pre-collisional geodynamic context of the southern margin of the Pan-African fold belt in Cameroon. J. Afr. Earth Sc. 99, 245–260.
Nomo, E.N., Tchameni, R., Vanderhaeghe, O., Sun, F., Barbey, P., Tekoum, L., Tchunte, P.M.F., Eglinger, A., Fouotsa, N.A.S., 2017. Structure and LA-ICP-MS zircon U-Pb dating of syntectonic plutons emplaced in the Pan-African Banyo-Tcholliré shear zone (central north Cameroon). J. Afr. Earth Sc. 131, 251–271.
Nzenti, J.P., Abaga, B., Suh, C.E., Nzolang, C., 2011. Petrogenesis of peraluminous magmas from the Akum-Bamenda Massif, Pan-African Fold Belt, Cameroon. Int. Geol. Rev. 53, 1121–1149.
Pearce, J.A., Harris, N.B.W., Tindle, A.G., 1984. Trace Element Discrimination Diagrams for the Tectonic Interpretation of Granitic Rocks. J. Petrol. 25, 956–983.
Pearce, J.A., Peate, D.W., 1995. Tectonic Implications of the Composition of Volcanic ARC Magmas. Annu. Rev. Earth Planet. Sci. 251–285.
Penaye, J., Kröner, A., Toteu, S.F., Van Schmus, W.R., Doumnang, J.-C., 2006. Evolution of the Mayo Kebbi region as revealed by zircon dating: An early (ca. 740Ma) Pan-African magmatic arc in southwestern Chad. J. Afr. Earth Sci. 44, 530–542.
Penaye, J., Toteu, S.F., Tchameni, R., Van Schmus, W.R., Tchakounté, J., Ganwa, A., Minyem, D., Nsifa, E.N., 2004. The 2.1Ga West Central African Belt in Cameroon: extension and evolution. J. Afr. Earth Sc. 39, 159–164.
Rapp, R.P., Shimizu, N., Norman, M.D., Applegate, G.S., 1999. Reaction between slab-derived melts and peridotite in the mantle wedge: experimental constraints at 3.8 GPa. Chem. Geol. 160, 335–356.
Rapp, R.P., Watson, E.B., 1995. Dehydration Melting of Metabasalt at 8–32 kbar: Implications for Continental Growth and Crust-Mantle Recycling. J. Petrol. 36, 891–931.
Rapp, R.P., Watson, E.B., Miller, C.F., 1991. Partial melting of amphibolite/eclogite and the origin of Archean trondhjemites and tonalites. Precambr. Res. 51, 1–25.
Rollinson, H.R., 1993. Using geochemical data: evaluation, presentation, interpretation. Longman Singapore Publisher (Pte) Ltd, Singapore, pp. 1–352.
Saha-Fouotsa, A.N., Vanderhaeghe, O., Barbey, P., Eglinger, A., Tchameni, R., Zeh, A., Tchunte, P.F., Nomo, E.N., 2019. The geologic record of the exhumed root of the Central African Orogenic Belt in the central Cameroon domain (Mbé – Sassa-Mbersi region). J. Afr. Earth Sc. 151, 286–314.
Shang, C.K., Siebel, W., Satir, M., Chen, F., Mvondo, J.O., 2004. Zircon Pb–Pb and U-Pb systematics of TTG rocks in the Congo Craton: constraints of crustal formation, crystallization and Pan-African lead loss. Bull. Geosci. 79, 205–2019.
Simeni, N.A.W., Tchato, D.T., Belnoun, R.N.N., Tchouankoue, J.P., Ganwa, A.A., 2017. Structural Relationship between Brittle Deformation and Paleozoic to Mesozoic Basalt Dykes in the Precambrian Basement of the Southern Continental Part of the Cameroon Volcanic Line. Int. J. Geosci. 318–331.
Smithies, R.H., Champion, D.C., 2000. The Archaean High-Mg Diorite Suite: Links to Tonalite–Trondhjemite–Granodiorite Magmatism and Implications for Early Archaean Crustal Growth. J. Petrol. 41, 1653–1671.
Sun, S.s., McDonough, W.F., 1989. Chemical and isotopic systematics of oceanic basalts: implications for mantle composition and processes. Geological Society, London, Special Publications 42, 313.
Tagne-Kamga, G., 2003. Petrogenesis of the Neoproterozoic Ngondo Plutonic complex (Cameroon, west central Africa): a case of late-collisional ferro-potassic magmatism. J. Afr. Earth Sc. 36, 149–171.
Tchakounté, J., Eglinger, A., Toteu, S.F., Zeh, A., Nkoumbou, C., Mvondo-Ondoa, J., Penaye, J., de Wit, M., Barbey, P., 2017. The Adamawa-Yadé domain, a piece of Archaean crust in the Neoproterozoic Central African Orogenic belt (Bafia area, Cameroon). Precambr. Res. 299, 210–229.
Tchameni, R., Pouclet, A., Penaye, J., Ganwa, A.A., Toteu, S.F., 2006. Petrography and geochemistry of the Ngaoundéré Pan-African granitoids in Central North Cameroon: Implications for their sources and geological setting. J. Afr. Earth Sc. 44, 511–529.
Tchaptchet Tchato, D., 2011. Geology of the Kekem area (Cameroon central domain): metamorphic petrology, P-T-t path, EMP (monazite) In: LA-ICPMS (zircon) dating and implications for the geodynamic evolution of the Pan-African North Equatorial fold belt. These de doctorat/PhD, 109.
Tchaptchet Tchato D., Schulz B., J.P, N., 2009. Electron microprobe dating and thermobarometry of. Neoproterozoic metamorphic events in Kekem area, central African Fold Belt of Cameroon. Neues Jahrbuch Mineral. 186, 95–109.
Tcheumenak Kouémo, J., Njanko, T., Kwékam, M., Naba, S., Bella Nké, B.E., Yakeu Sandjo, A.F., Fozing, E.M., Njonfang, E., 2014. Kinematic evolution of the Fodjomekwet-Fotouni Shear Zone (West-Cameroon): Implications for emplacement of the Fomopéa and Bandja plutons. J. Afr. Earth Sci. 99, 261–275.
Tchouankoue, J.P., Li, X.-H., Belnoun, R.N.N., Mouafo, L., Ferreira, V.P., 2016. Timing and tectonic implications of the Pan-African Bangangte syenomonzonite, West Cameroon: Constraints from in-situ zircon U-Pb age and Hf-O isotopes. J. Afr. Earth Sci. 124, 94–103.
Tchouankoue, J.P., Simeni Wambo, N.A., Kagou Dongmo, A., Li, X.-H., 2014. 40Ar/39Ar dating of basaltic dykes swarm in Western Cameroon: Evidence of Late Paleozoic and Mesozoic magmatism in the corridor of the Cameroon Line. J. Afr. Earth Sci. 93, 14–22.
Tchuimegnie Ngongang, N.B., Kamgang, P., Chazot, G., Agranier, A., Bellon, H., Nonnotte, P., 2015. Age, geochemical characteristics and petrogenesis of Cenozoic intraplate alkaline volcanic rocks in the Bafang region, West Cameroon. J. Afr. Earth Sci. 102, 218–232.
Toteu, S.F., Penaye, J., Djomani, Y.P., 2004. Geodynamic evolution of the Pan-African belt in central Africa with special reference to Cameroon. Rev. cannadienne des sciences de la terre 73–85.
Toteu, S.F., Van Schmus, W.R., Penaye, J., Michard, A., 2001. New U-Pb and Sm–Nd data from north-central Cameroon and its bearing on the pre-Pan African history of central Africa. Precambr. Res. 108, 45–73.
Trompette, R., 1997. Neoproterozoic (~600 Ma) aggregation of Western Gondwana: a tentative scenario. Precambr. Res. 82, 101–112.
Ugwuonah, E.N., Tsunogae, T., Ekwueme, B.N., 2019. Petrology and phase equilibrium modeling of granulites from Obudu in the Benin-Nigerian Shield, Southeastern Nigeria: implications for clockwise P-T evolution in a collisional orogen. Mineral. Petrol. 113, 353–368.
van de Flierdt, T., Frank, M., Lee, D.-C., Halliday, A.N., 2002. Glacial weathering and the hafnium isotope composition of seawater. Earth Planet. Sci. Lett. 201, 639–647.
Vervoort, J.D., Jonathan Patchett, P., 1996. Behavior of hafnium and neodymium isotopes in the crust: Constraints from Precambrian crustally derived granites. Geochim. Cosmochim. Acta 60 (19), 3717–3733.
Vervoort, J.D., Patchett, P.J., Albarède, F., Blichert-Toft, J., Rudnick, R., Downes, H., 2000. Hf–Nd isotopic evolution of the lower crust. Earth Planet. Sci. Lett. 181, 115–129.
Villaseca, C., Barbero, L., Herreros, V., 1998. A re-examination of the typology of peraluminous granite types in intracontinental orogenic belts. Trans. Roy. Soc. Edinburgh: Earth Sci. 89, 113–119.
Wang, W., Pandit, M.K., Zhao, J.H., Chen, W.T., Zheng, J.P., 2018. Slab break-off triggered lithosphere - asthenosphere interaction at a convergent margin: The Neoproterozoic bimodal magmatism in NW India. Lithos 296-299, 281–296. https://doi.org/10.1016/j.lithos.2017.11.010.
Whattam, S.A., Gazel, E., Yi, K., Denyer, P., 2016. Origin of plagiogranites in oceanic complexes: A case study of the Nicoya and Santa Elena terranes, Costa Rica. Lithos 262, 75–87.
Winchester, J.A., Floyd, P.A., 1976. Geochemical magma type discrimination: application to altered and metamorphosed basic igneous rocks. Earth Planet. Sci. Lett. 28, 459–469.
Wu, R.-X., Zheng, Y.-F., Wu, Y.-B., Zhao, Z.-F., Zhang, S.-B., Liu, X., Wu, F.-Y., 2006. Reworking of juvenile crust: Element and isotope evidence from Neoproterozoic granodiorite in South China. Precambr. Res. 146, 179–212.
Zhang, Z., Zhao, G., Santosh, M., Wang, J., Dong, X., Shen, K., 2010. Late Cretaceous charnockite with adakitic affinities from the Gangdese batholith, southeastern Tibet: Evidence for Neo-Tethyan mid-ocean ridge subduction? Gondwana Res. 17, 615–631.